2006

Internal magnetic field distribution of a type II high Tc superconductor with non-conducting inclusions

Yuxin Dai

College of William & Mary - Arts & Sciences

Internal Magnetic Field Distribution of a Type II High T_c

Superconductor with Non-conducting Inclusions

_____

A Dissertation

Presented to

The Faculty of the Department of Physics

The College of William & Mary in Virginia

In Partial Fulfillment

Of the Requirements for the Degree of

Doctor of Philosophy

_____

by

Yuxin Dai

2006

APPROVAL SHEET

This dissertation is submitted in partial fulfillment of

the requirements for the degree of

Doctor of Philosophy

Yuxin Dai

Approved, August 2006
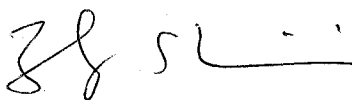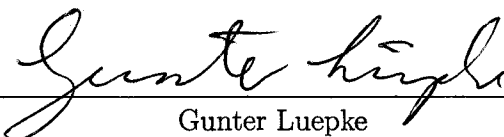
William J. Kossler
Thesis Advisor

Kenneth G. Petzinger
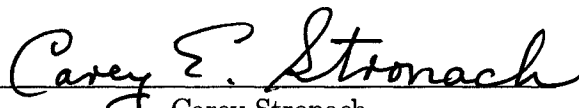
Shiwei Zhang

Gunter Luepke

Carey Stronach
Virginia State University

ii

To my parents, family members and friends in China and U.S.

Table of Contents

v

ACKNOWLEDGMENTS

First of all, I would like to thank my advisor Professor William Jack Kossler for his insightful advices, kindness, patience, understanding and support of my research especially during these years while I work part time on my thesis.

I would also like to thank Professor Kenneth Petzinger, he reviewed several versions of my thesis and provided me with many valuable suggestions; thanks Professor Shiwei Zhang for his review and suggestions; thanks Professor Gunter Luepke for his review and suggestions; thanks Professor Carey Stronach for his review and suggestions, and thanks all commit members for their advice and comments.

Special thanks for Professor J. Dirk Walecka for teaching us Advanced Quantum Field Theory and General Relativity; it is always an inspiration and enjoyable experience to take his classes.

The experimental part of the thesis was done at TRIUMF in Vancouver, Canada; I would like to thank the support people there for their help.

Finally, I am most grateful for my family members and friends in US and China for their support and encouragement on my work.

List of Figures

ABSTRACT

The internal magnetic field distributions for a type II superconductor (a single crystal $YBa_2Cu_3O_{7-\delta}$) with large normal inclusions (Y_2BaCuO_5) are studied. A model based on the London Equations has been successfully developed and applied to the interpretation of the μSR data on this system. In our model, these inclusions are assumed to be cylindrical in shape and infinite in length. Therefore, this model should be especially appropriate for the prediction of field distributions in single crystal superconductors in which columnar defects have been purposely introduced to enhance pinning.

μSR experiments on a large single crystal sample of $YBa_2Cu_3O_{7-\delta}$ with non-conducting Y_2BaCuO_5 inclusions show some interesting characteristics, especially the magnetic field distribution in the inclusion regions. In our model, the difference between the field value in the inclusions and the value at the saddle point is sensitive to the penetration depth. Comparing the calculated to observed field differences provides a new method of determining the penetration depth.

Internal Magnetic Field Distribution of a Type II High T_c Superconductor with Non-conducting Inclusions

Chapter 1

Introduction

The magnetic flux structures in superconductors show interesting properties in the presence of an applied magnetic field. In 1933 Meissner and Ochsenfeld [1]observed complete expulsion of magnetic field from a superconducting material placed in a weak magnetic field, now known as the Meissner effect. However this complete flux expulsion only occurs when the magnetic fields are weak and/or the demagnetizing effects are small. When these conditions are not met, for example when the applied magnetic field is strong enough or the demagnetization effects cannot be ignored such as for a thin superconducting disk placed perpendicular to the applied magnetic field, then the magnetic flux penetrates part of the superconducting material, and as a result, the material divides into normal and superconducting domains.

The domain structures in superconductors in the presence of applied magnetic fields possess interesting properties. There is an energy associated with the interface between the normal and superconducting regions that is called the wall energy. The wall energy can be either positive or negative. When the wall energy is positive, the amount of quantum flux, $\Phi_0 = \frac{hc}{2e} = 2.07 \times 10^{-7} Gcm^2$, contained in a single domain can be greater than one. This type of material is called type I superconductor. The domain structure of type I

2

superconductor is referred to as intermediate state [2]. When the wall energy is negative, the magnetic flux can only penetrate the superconducting material in the form of a single flux quanta Φ_0. This type of superconducting material is called a type II superconductor. The domain structure of type II superconductors is referred as the mixed state [3, 4],[5].

Muons were used as probes of magnetism in matter as early as 1944 [6]. However, it was the discovery of the violation of parity symmetry in Kaon decay by Lee and Yang in 1956 [7] that made the properties of muons clearly understood, and opened the way for widely using muon as probes of matter. The parity nonconservation decay of a π^+ (π^-) produces a μ^+ (μ^-) which has a large asymmetry when it decays. The e^+ (e^-) is emitted preferentially along (opposite to) the muon spin direction. The experiments of Garwin et al. [8], Friedman and Telegdi [9], and Wu et al.[10] not only confirmed Lee and Yang's theory, but also suggested that the asymmetry of positive μ^+ decays could be used as a probe for the magnetism of matter.

Negative muons are rarely used, because after being stopped in a sample, they normally undergo nuclear capture from a low-lying orbital of muonic atoms before they have a chance to decay.

The modern μSR technique - Moun Spin Rotation (μSR also stands for Muon Spin Relaxation and Resonance, but here we are only interested in Moun Spin Rotation) most commonly uses a transverse magnetic field (TF), applied perpendicular to the muon polarization; The muon spins then precess about the internal magnetic field of the magnetic material. TF-μSR has been widely used to study the magnetic flux structures of High Temperature Superconductors among other materials. We use μSR technique to study the temperature dependence of London penetration depth of the type II high T_c superconduct-

ing material.

The temperature dependence of London penetration depth is of particular interest since at low temperature it reflects changes in the superfluid density which is responsible for the screening of electric magnetic field. The energy gap in the excitation spectrum of a BCS paring state shows exponential temperature dependence at low temperature. In s-wave BCS paring the deviation of London penetration depth from its zero temperature value follows [12] $\lambda(T) - \lambda(0) \sim (\frac{T_c}{T})^{1/2} exp(-1.76 T_c/T)$. By studying the temperature dependence of London penetration depth we can study the deviation from BCS s-wave paring, therefore, the measurement of temperature dependence of magnetic penetration depth provide an experimental method to study the unconventional BCS paring state.

Microwave techniques have been commonly used for measuring of the temperature dependence of the penetration depth.

Unlike other techniques, the μSR provides a microscopic measure of the flux lines dynamic and is a powerful tool to study the magnetic field properties of superconducting material. The study in this paper provides a new method to determine the temperature dependence of the London penetration depth of a type II superconducting material with nonconducting inclusions using μSR techniques.

It has become possible to grow large single crystals of $YBa_2Cu_3O_{7-\delta}$ with Y_2BaCuO_5 inclusions [11]. These crystals have strong pinning, can carry large currents, trap large fields and provide moderately strong levitation forces on magnets. Because of these properties this material is thought to be advantageous for a variety of practical applications[13, 15].

The included non-superconducting material, "green-phase" Y_2BaCuO_5, is needed to provide a source of Y as the crystal grows. The internal magnetic fields in pure Y_2BaCuO_5

have been observed in the zero-field μSR study of Weidinger *et al.*[16]. These authors

observe at least 5 different fields and an ordering temperature of about 15 K. Mössbauer

effect studies[17] have observed this material to order magnetically at about 15.5(3) K.

Neutron scattering[18] has found this ordering to be 3D anti-ferromagnetic and to occur at

16.2(5) K.

Muon spin rotation, μSR, has been used to measure internal magnetic field probability

distributions, $n(h)$, for a large single crystal of $YBa_2Cu_3O_{7-\delta}$ with non-superconducting

inclusions. For pure $YBa_2Cu_3O_{7-\delta}$, when the applied field is parallel to the **c** axis of

the crystal, this would be expected to have a single peak[22], below the applied field,

corresponding to the saddle point of the magnetic field spatial distribution. However, our

YBCO sample showed two peaks: a left peak, which is below the applied field and at the

saddle point field as expected for a pure YBCO sample; and a right peak, which is above

the applied field, see Fig.1.1. We argue that the right peak reflects the magnetic field

distribution in the non-conducting Y_2BaCuO_5 inclusions. The separation between the two

peaks goes to zero near the transition temperature(90 K), and reaches 50 Gauss at 18 K.

Below 18 K the green phase material undergoes a transition to an antiferromagnetic state.

In these now antiferromagnetic inclusions randomly directed large fields take the muon

precession signal out of our frequency window. The data shown in Fig.1.1 indicate that the

volume of the inclusions could be up to 20 percent of the total volume of the sample.

In the this study we seek to characterize the microscopic internal magnetic field distri-

butions in these materials, including the effects of large inclusions. When inclusions are not

present, it has been found that the London equation is a good approximation in describing

magnetic fields and magnetic properties of type II superconducting materials for applied
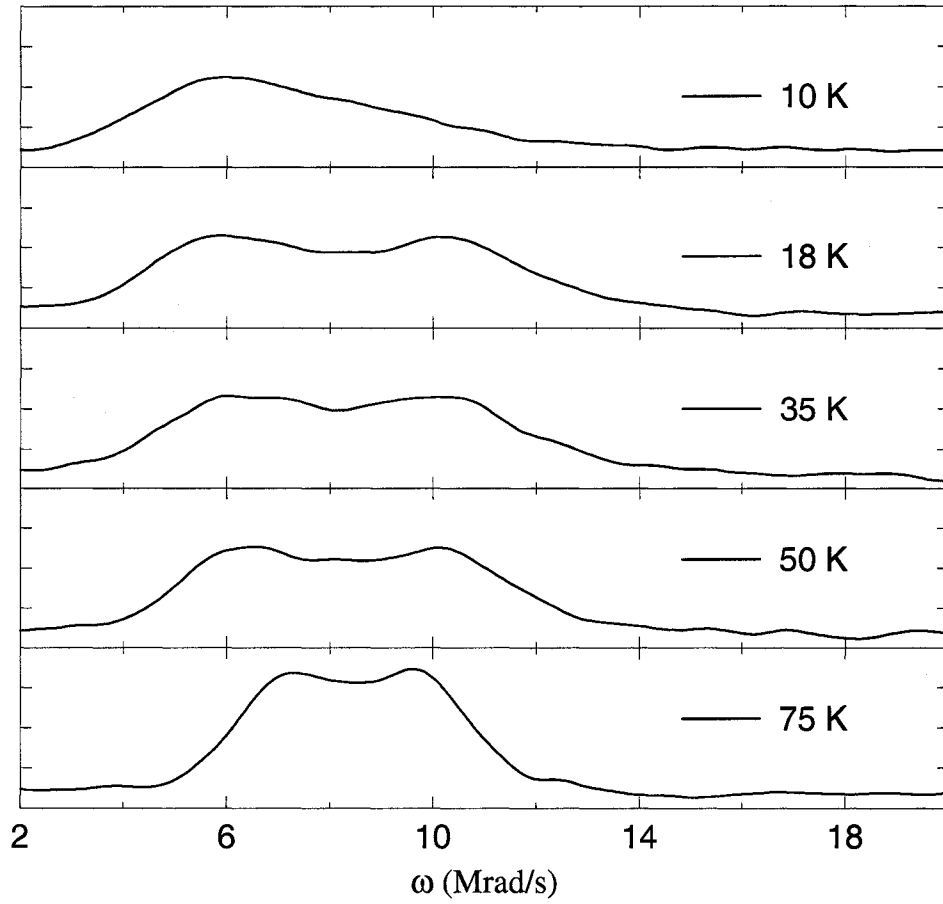
Figure 1.1: Fourier transformations of μSR data on a single crystal $YBa_2Cu_3O_{7-\delta}$. The applied field was 100 Gauss($\omega = \gamma_\mu h$), and was parallel to the crystal c axis. The left peak corresponds to the saddle point of the magnetic field distribution. The right peak corresponds to the internal magnetic distribution inside non-conducting inclusions.

fields in the range of $H_{c_1} < H < H_{c_2}$, where H_{c1} and H_{c2} are lower and higher critical field of type II superconducting material, respectively. We have developed a model based on the London equations with the following assumptions: 1). the "green phase" inclusions are cylindrical and infinite in length; 2). they are non-conducting; 3). they do not change the overall vortex lattices structure so that the near neighbors are still hexagonally arranged; 4). for a given temperature, the more distant vortices contribute a constant average field

within the hexagonal array, and this filed is ignored in the model.

Assumptions 1 and 2 are basic assumptions of the model to be discussed, and are generic. Assumption 3 and 4, as one can see in chapter 6 where the model is compared with μSR experiment, are good approximations for the lower applied magnetic field case. When the applied field is too high, for example when vortex spacing is less than the penetration depth, assumptions 3 and 4 may need to be modified. Also, since inclusions provide strong pinning, possible temperature modification of the vortex density is not considered in our model.

In our model the separation between the two peaks in Fig.1.1 depends on the assumed inclusion radius and penetration depth λ. We can independently determine λ just below 18 K where the second peak disappears, and then use this value at 18 K to determine the inclusion size. Then, with this now known inclusion radius we can determine the temperature dependence of the penetration depth from the variation of the separation between the two peaks. This provides a new method to measure the temperature dependence of the penetration depth[14].

This paper is organized as follows. In Chapter 2, we briefly review μSR techniques and our experimental set up for measuring the internal magnetic field distribution. In chapter 3, we briefly discuss the Intermediate State, Mixed State and the London Model. In chapter 4, we calculate the magnetic field and energy of an isolated cylindrical non-conducting inclusion with a flux vortex trapped in its center, and compare with that of a free isolated vortex line. Interaction between a cylindrical inclusion and a vortex line is also obtained. In Chapter 5, we consider the case that is closer to the experimental environment, a cylindrical inclusion surrounded by hexagonally placed superconducting vortices. The model and μSR experimental data will be compared in Chapter 6.

Chapter 2

μSR Experiment

2.1 μSR techniques

2.1.1   Muon production

In μSR experiments we use muons to probe the magnetic properties of matter. This requires that muons stop in the sample. Muons produced from various high-energy process and elementary particle decays normally have much higher energy, which prevents them from stopping in a sample of normal thickness used in the μSR experiments. In order for muons to stop in the sample of thickness of a few mm, the incoming μ^+ beam must have a relatively low energy. These low energy μ are available from the two-body decay of charged pions stopped near the surface of the pion production target − these muons are called *surface muons*.

In the two-body pions decay, a pion decays into a muon and a neutrino.

$$\pi^+ = \mu^+ + \nu_\mu;$$

$$\pi^- = \mu^- + \bar{\nu}_\mu; \tag{2.1}$$

8

Where ν_μ is the neutrino associated with μ^+, and $\bar{\nu}_\mu$ is the antineutrino associated with μ^-.

A muon produced in the rest frame of the pion has a kinetic energy of 4.119 MeV and a momentum of 29.79 MeV/c. This low kinetic energy allows muon to have a short range, and thus to stop in thin samples.

Since a π^- stopping in the production target normally undergoes nuclear capture from low-lying orbital of a pionic atom before it has chance to decay, a *surface* beam of μ^- is not practical. Therefore, most of the muon beams used in μSR experiments today are produced by π^+ decay.

2.1.2   Spin Polarization of Muon

We know that in nature the neutrino has only negative helicity in which its spin is antiparallel to its momentum, and the antineutrino is only produced with positive helicity in which its spin is parallel to its momentum. Thus, the conversation of both linear and angular momentum requires that the μ^+ have negative helicity. Therefore, in the rest frame of pion, the μ^+ emitted from π^+ decay is 100 percent spin polarized opposite to the direction of its momentum. This gives μSR the great advantage of using a perfectly polarized probe.

2.1.3   Muon Decay

In its rest frame, a muon has a life-time of 2.19 μs. A positive muon decays into a positron, a neutrino and an antineutrino:

$$\mu^+ = e^+ + \nu_e + \bar{\nu}_\mu; \tag{2.2}$$

where ν_e is the neutrino associated with the electron and $\bar{\nu}_\mu$ is the antineutrino associated with the muon.

Due to parity non-conversation in weak interactions, the positron produced in 3 body muon decay is emitted with an asymmetric angular distribution relative to μ^+ spin. Therefore, by recording the angular distribution of emitted positrons, one can read out the spin polarization of muons at the moment of decay. This property is critically important to μSR experiments.

The probability distribution P(θ) of the muon decay depends on the energy of positron $x = \frac{E_e}{E_{max}}$ (E_{max}=52.83 MeV is the maximum possible total energy of the positron,and E_e is the positron energy), as well as the angle θ between the positron emitting direction and muon spin direction[31].

$$dP(\theta) = E(x)[1 + a(x)cos\theta]dxd(cos\theta). \tag{2.3}$$

where a(x) is the asymmetry factor:

$$a(x) = \frac{2x - 1}{3 - 2x}, \tag{2.4}$$

and $E(x) = 2x^2(3 - 2x)$ is normalized e^+ or e^- energy spectrum.

2.1.4 Muon Rotation

The muon is a fermion with spin quantum number equal to $\frac{1}{2}$. It has a magnetic moment of

$$\mu_\mu = 1.001165932 \frac{e\hbar}{2m_\mu c}. \tag{2.5}$$

where m_μ is the mass of Muon.

In presence of a magnetic field, muons will experience a torque

$$\vec{\tau} = \vec{\mu} \times \vec{H}. \tag{2.6}$$

Since the torque is equal to the time rate of change of the muon's spin angular momentum

$$\vec{\tau} = \frac{d\vec{S}}{dt}, \tag{2.7}$$

we have

$$\frac{d\vec{S}}{dt} = \vec{\mu} \times \vec{H}, \tag{2.8}$$

which means that the muon's spin will rotate(precess) about the direction of the local

magnetic field $\vec{H}$, see Fig.2.1.
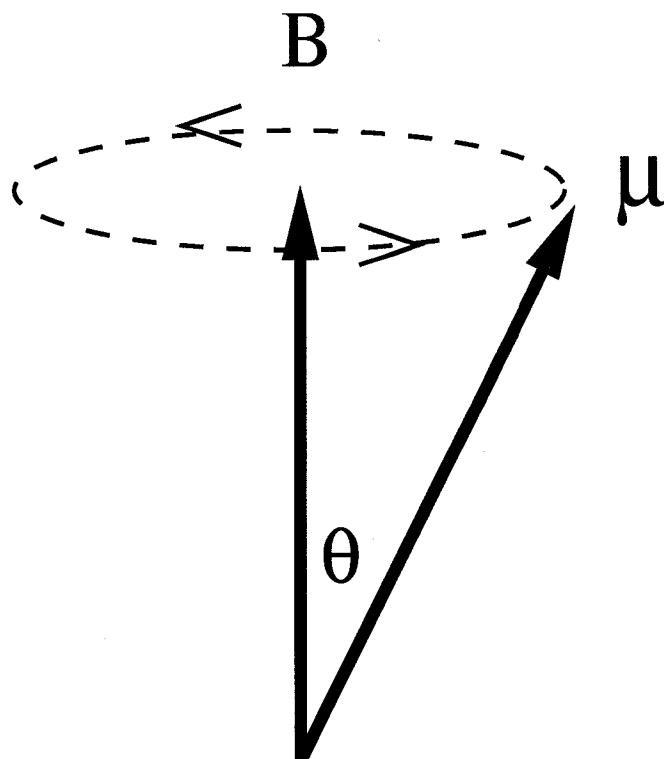
Figure 2.1: Muon spin rotate about the direction of the external magnetic field.

2.1.5 Time Differential μSR

Ideally, in a μSR experiment, one wants to count one μ^+ decay event at a time. A time to digital converter(TDC) is used to digitize the time difference between a μ^+ stop and the detection of the decay e^+. Events are only recorded if the μ^+ stop is not preceded or followed by a second μ^+ within 10 μS, and if only one e^+ occurs in the time following the μ^+ stop.

Fig.2.2 shows a typical experimental set up in a TD-μSR. For simplicity, the Helmholtz coils to produce external magnetic field are not shown. In Fig. 2.2, B is the backward positron detector and F is the forward detector. S is a scope scintillator, and V is a veto
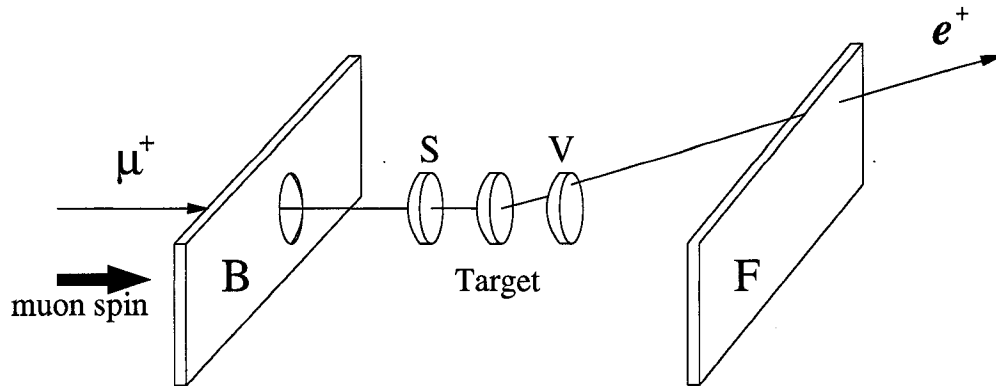
Figure 2.2: μSR experimental setup

scintillator. S and V are placed very close to the sample. When a μ^+ traverses S, a signal

will be generated. If the μ^+ does not stop in the sample, a second signal will be generated

shortly in V when it traverses the veto scintillator, the event then will be discarded. If μ^+

does stop in the sample, the signal from S will then start the TDC.

2.1.6   Time-Differential μSR in Transverse Field

The most commonly used time-differential μSR is the transverse field(TF) μSR. In TF-μSR,

a magnetic filed $\vec{H}$ is applied perpendicular(transverse) to the initial muon spin polarization,

causing Larmor precession of the muon spin about the direction of the applied field $\vec{H}$. There

may be as many as six positron detectors arranged around the sample. Defined to their

position relative to the incoming muon beam, they are called Forward(F), Backward(B),

Up(U), Down(D), Left(L), and Right(R). Depending on the orientation of the applied field

and μ^+ polarization, at least two of those six detectors will record muon precession frequency

signals,

$$\omega = \gamma_\mu h \qquad (2.9)$$

where $\gamma_\mu = 2\pi \cdot 135.5 MH_z T^{-1}$ is the gyromagnetic ratio of muon spin, and h is the local

magnetic field where muon stops. Since the muon precession frequence is directly observable

in a μSR experiment,the local magnetic field where muon stops can be determined.
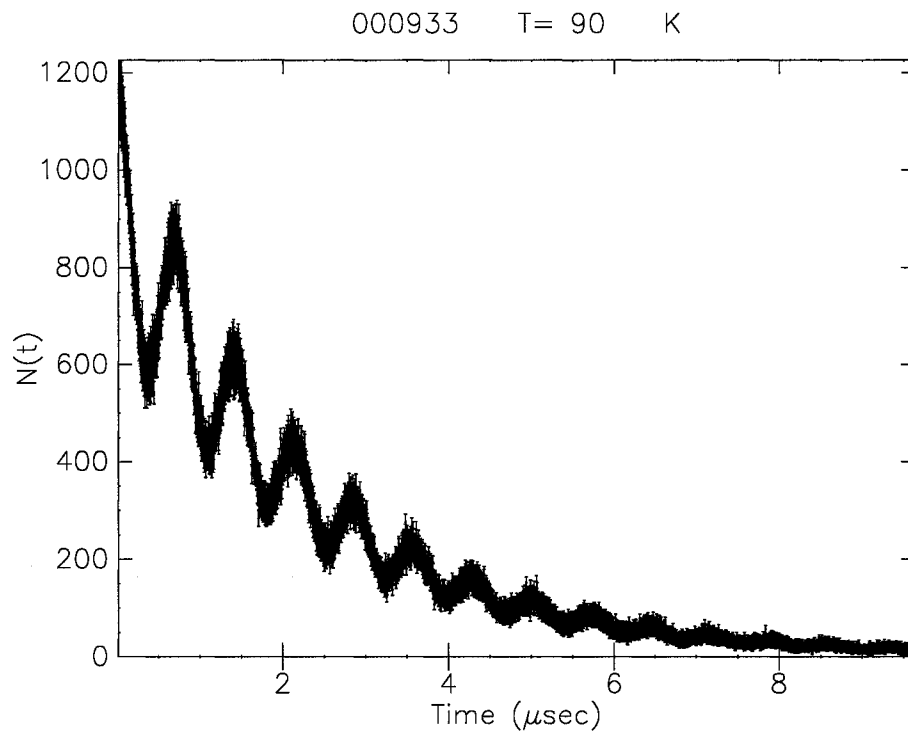
Figure 2.3: Real time spectrum from a TF-μSR experiment.

Fig.2.3 shows the histogram from a TF-μSR experiment. The muon lifetime is reflected

in the overall exponential decay. The oscillation superimposed on the exponential curve is

produced by the Larmor precession of the μ^+ spin about the local magnetic field $\vec{h}$.

Fig.2.4 shows the asymmetry spectrum from the same set of data as in Fig.2.3. The

background exponential decay has been subtracted.
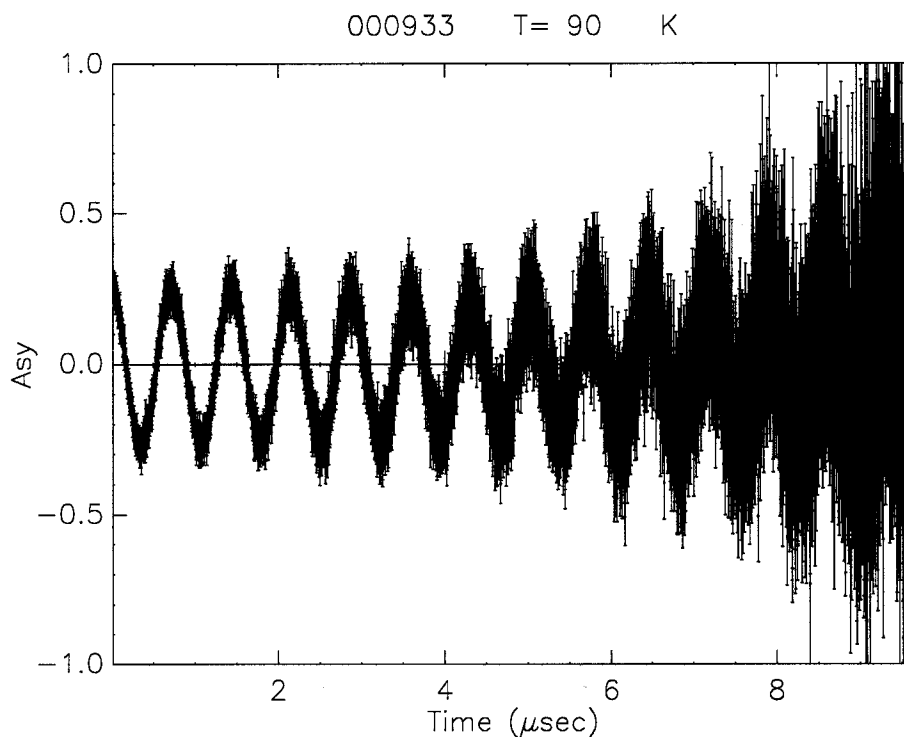
Figure 2.4: An asymmetry spectrum of Fig.2.3.

Often one needs to analyze the μSR data in the frequency domain rather than in the time domain. A Fourier Transform is employed for this purpose. Fig.2.5 shows the Fourier Transform(FT) of the μSR data as shown in real time space in Fig.2.4. Both real part(top) and imaginary part(bottom) of the Fourier amplitude are shown in Fig.2.5.
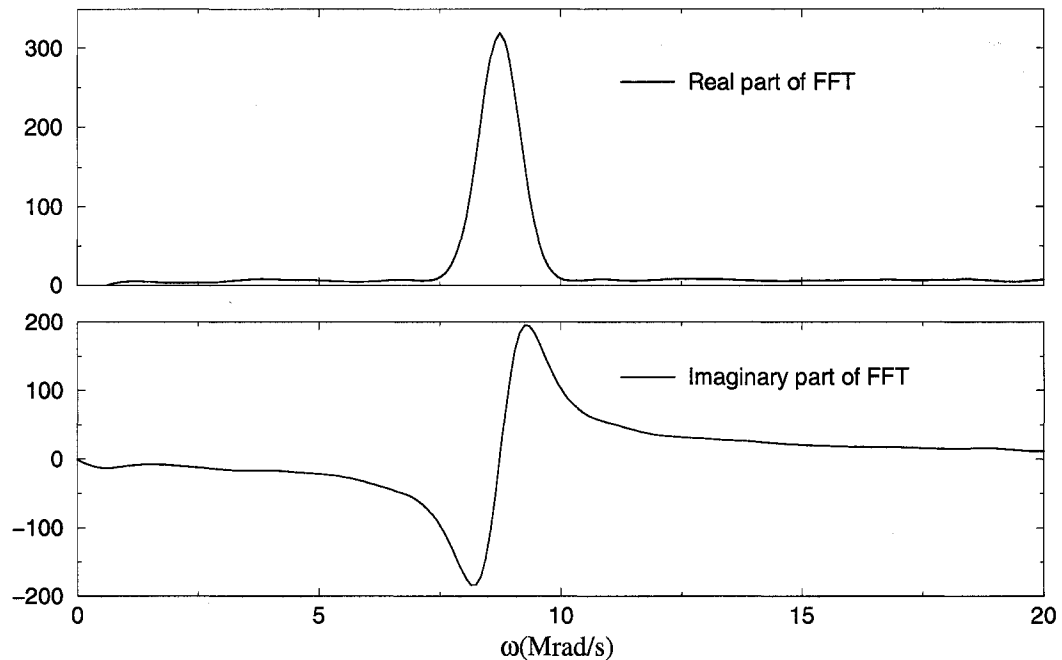
Figure 2.5: Complex Fourier transform of the real time μSR data in fig. 2.4.

2.2　Experimental

The experiments were carried out at the TRIUMF facility in Vancouver, BC, using the M20 beam line of polarized muons. The muons were spin rotated and we measured their polarization to be approximately 14 degrees from vertical; that is they were spin-rotated by about 76 degrees.

The single crystal $YBa_2Cu_3O_{7-\delta}$ sample with non-conducting Y_2BaCuO_5 inclusions was provided by M. Strasik of Boeing. It was mounted with its c axis parallel to the incoming beam in a horizontal cryostat which used flowing H_e vapor to provide cooling. Temperature was monitored by means of a LakeShore GaAlAs Diode near the sample and was accurate to less than 0.1 K.

A pair of Helmholtz coils provide up to 5 kG magnetic filed with its axis parallel to the

incoming beam and crystal **c** axis. The experiments that are reported here were carried out at approximately 100 Gauss. The fields were measured by a Hall probe, but ultimately were determined by the μSR itself. That is, above T_c the precession frequency was used. At the field used the atomic position scale, which determines where the muon stops, is much smaller than the penetration depth, vortex spacing, or inclusion size. Thus, one may assume the muon to sample the internal fields uniformly.

Since the sample was a thin plate placed perpendicular to the applied field, the demagnetization coefficient is near 1.0 [19]. This means that the applied magnetic field will penetrate the sample even if it is much lower than the lower critical field H_{c1}. The field is applied before the temperature is lowered through T_c. At temperatures slightly below T_c the vortices become pinned in YBCO which does not allow any field to escape as the temperature is lowered, thus the average field inside should be very close to the applied field.

The present measurements were transverse field measurements. While forward, backward, up, and down positron detectors were in place, only the up and down detectors were used for the measurements described here. Calling the up-detector time-histogram after subtracting background: U(t), and for the corresponding down-detector: D(t), we obtained the asymmetry function from:

$$A(t) = \frac{U(t) - \alpha D(t)}{U(t) + \alpha D(t).} \qquad (2.10)$$

In this equation α is a factor to correct for relative detector efficiencies. From these we obtained the cosine and sine Fourier transforms, using the above T_c data to determine the appropriate phase so that the cosine transform is the field distribution n(h):

$$n(h) \propto \int \cos(\gamma_\mu ht) A(t) dt \qquad (2.11)$$

in which γ_μ is the muon's gyromagnetic ratio, and h is the local magnetic field. The proportional constant can be easily obtained by requiring that n(h) integrate to unity.

For a crystal without inclusions we have been able to fit the $n(h)$ to that produced by a triangular vortex lattice for which the effects of pinning are treated by varying the local average field with a Gaussian distribution function of variance σ. The effects of finite core size and longitudinal vortex disorder are included by means of a Debye-Waller factor[20] in the reciprocal lattice sum. Here for simplicity the Debye-Waller factor was set to a small value. Also it should be noted that this factor tends to narrow the Fourier transform distribution. These field calculations follow closely the method described by Thiemann et al.,[21]. For more details on our calculation see the monograph of Greer and Kossler[22].

Chapter 3

Intermediate State, Mixed State

and London Model

The complete flux expulsion(Meissner State) from a superconductor happens only when the magnetic fields are weak or the demagnetization factor is small. The Meissner State occurs in type I superconductors when the applied field H is less than the critical field H_c under the condition that the demagnetization factor is negligible. If the demagnetization factor D is appreciable, magnetic flux starts to penetrate the superconducting material even if the applied field is less than the critical field, but greater than $H_c(1\text{-}D)$.

For type II superconductors, magnetic flux starts to penetrate when the applied field H is greater than the lower critical field H_{c_1} when the demagnetization factor can be ignored. If the demagnetization factor is appreciable, magnetic flux starts to penetrate the superconducting material even if the applied field is less than the lower critical field, but greater than $H_{c_1}(1\text{-}D)$. A type II superconductor goes into the mixed state when the applied field is in the range of $H_{c_1}(1 - D) < H < H_{c_2}$. Because the wall energy of type II superconductor is negative, the magnetic flux can only penetrate the material in the form of single flux quanta Φ_0.

19

3.1 Gibbs free energy

The first law of thermodynamics for materials with magnetization $\vec{M}$ in applied magnetic field $\vec{B}$ can be written as

$$dU = TdS + \vec{B} \cdot d\vec{M} \tag{3.1}$$

where dU is the differential of internal energy, T is the temperature, and S is the entropy.

We then get the Gibbs free energy,

$$dF = -SdT - \vec{M} \cdot d\vec{B}. \tag{3.2}$$

Assuming isothermal conditions, dT = 0; The Gibbs free energy becomes

$$dF = -\vec{M} \cdot d\vec{B}. \tag{3.3}$$

The material magnetization $\vec{M}$ is directly linked to the thermodynamic critical field H_c, at that point the superconducting state becomes energetically unfavorable. The difference of free energy in the normal phase $F_n(T)$ and in superconducting state $F_s(T)$ in zero magnetic field is

$$(F_n(T) - F_s(T))|_{h=0} = -\int_0^{H_c} \vec{M}(h)dh. \tag{3.4}$$

From the above, we can determine the thermodynamic critical field H_c,

$$(F_n(T) - F_s(T))|_{h=0} = \frac{H_c(T)^2}{8\pi}. \tag{3.5}$$

Thus it is energetically favorable to transfer from the normal phase to superconducting phase. The unit volume of condensation energy gained through this phase transfer is $\frac{H_c(T)^2}{8\pi}$.

3.2   Wall energy

Complete flux expulsion from superconductors only happens when the demagnetization effect is negligible. When this condition is not met, such as when a thin superconducting plate is placed perpendicular to the external magnetic field, magnetic flux will penetrate the superconducting materials. The demagnetization effect results in a field at the edge of the sample that is

$$H' = \frac{H}{1-D},$$ (3.6)

where $0 < D < 1$ is the demagnetization coefficient.

The demagnetization effectively reduces the critical field H_c to $H_c(1-D)$. So when the field is greater than $H_c(1-D)$, the superconductor splits into normal and superconducting domains, see Fig.3.1. Such a mixture of normal and superconducting states is called the intermediate state or mixed state, which will be discussed in detail in the next two sections.

The energy associated with the interface between the normal and superconducting state is called the wall energy. The wall energy is closely related with the condensation energy. Let's consider the interface between a normal and superconducting domain. The super-conducting electron density and magnetic field at the interface between the normal and superconducting domains is shown in Fig.3.2.

On the left hand side of Fig.3.2, the superconducting electron density n_s decreases to zero at the S-N interface – the distance over which this occur is approximately equal to the coherence length ξ. The decrease of n_s reflects the loss of condensation energy, which makes a positive contribution to the wall energy. Since the unit volume condensation energy is
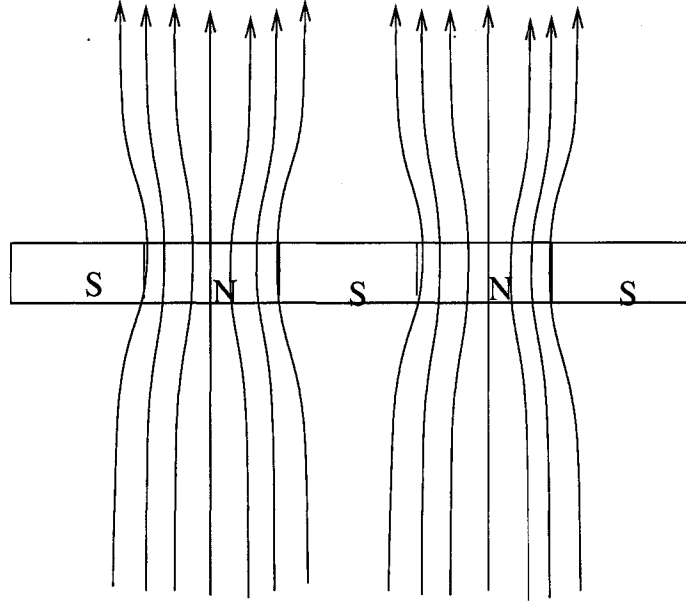
Figure 3.1: The mixture of normal and superconducting domains.

$\frac{H_c^2(T)}{8\pi}$, the contribution to the wall energy is $\frac{H_c^2(T)}{8\pi}\xi$.

On the right hand side of the S-N interface in Fig.3.2, the external magnetic filed penetrate S-N interface to the superconducting domain; the distance is characterized by the penetration depth λ. The associated energy is proportional to $\frac{H_c^2(T)}{8\pi}\lambda$. This part of the energy will enhance the condensation energy, this makes the negative contribution to the wall energy.

From the above discussion, we can define the wall energy as

$$E_w = \frac{H_c^2(T)}{8\pi}(\xi - \lambda).$$

(3.7)
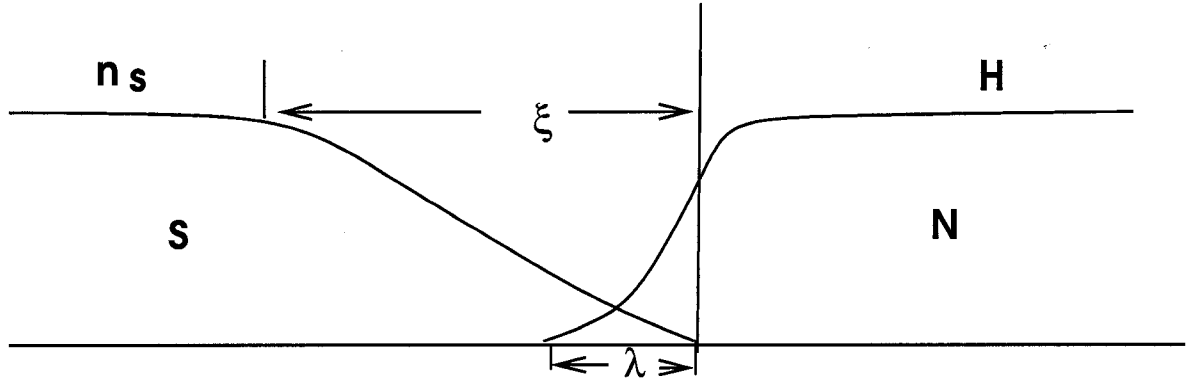
Figure 3.2: Superconducting electron density and magnetic field near the normal and superconducting interface .

3.3 Type-I superconductor and Intermediate State

For a superconducting material, if $\xi > \lambda$, then the wall energy is positive, this type of material is called type-I superconductor. The co-existence of normal and superconducting states in type-I superconductors is called the intermediate state.

Since the wall energy of type-I superconductors is positive, this indicates that in intermediate states it is energetically favorable to form normal domains with large dimensions in order to minimizes the areas of interface between S-N. Those large domains can contain many flux quanta.

A type I superconductor in the Meissner State has zero internal magnetic field, $B_{in}=0$. From a general relation of B and H field,

$$B_{in} = (H_{in} + 4\pi M) \tag{3.8}$$

where M is the material magnetization. Given Eq. 3.8, for Meissner state, we have

$$M = -\frac{1}{4\pi}H_{in},$$

$$H_{in} < B_c. \tag{3.9}$$

When $H_{in} > B_c$, magnetic flux starts to penetrate the material, and the superconductor goes into Intermediate State, where

$$B_{in} - B_c = 4\pi M, \tag{3.10}$$

3.4   Type-II Superconductor and Mixed State

If $\xi < \lambda$, the material is called a type-II superconductor. The wall energy of type-II superconductors is negative, which implies that it is energetically favorable to form many small domains such that each contains single flux quantum to maximized the interface areas between S-N.

When the applied field is less than the lower critical field and the demagnetization factor can be ignored, the Meissner State is observed in type II superconductor with

$$B_{in} = 0;$$

$$H_{in} = -4\pi M. \tag{3.11}$$

When the applied field is greater than the lower critical field H_{c_1}, the material goes into the mixed state, where the magnetic flux penetrates the superconductor in the form of vortex lines, each carrying a single flux quantum Φ_0. The material remains in the mixed state when the applied field is in the range of $H_{c_1} < H < H_{c_2}$. Superconductivity disappears when the field exceeds the upper critical field H_{c_2}.

Abrikosov first predicted the existence of a mixed state in type II superconductors where flux lines are arranged in the from of triangular lattice. This prediction has been verified by a number of experiments[23, 24].

To qualitatively understand the vortex state in type II superconductors, one needs to employ Ginzburg-Landau Theory[4]. However, a simple theoretical model (London Model) based on the London Equations is sufficient to describe the vortex state in the limit of $\kappa \gg$

1, where κ is the Ginzburg-Landau parameter

$$\kappa = \frac{\lambda(T)}{\xi(T)}. \qquad (3.12)$$

3.5 Two Fluid Model

Two fluid model was proposed by C. J. Gorter and H. B. C. Casimir [29] to account with the observed second order phase transition of superconductor at T_c. In two fluid model the total electron density is divided into superconducting electron density n_s and normal electron density n_n.

$$n = n_s + n_n. \tag{3.13}$$

The fraction $\frac{n_s}{n}$ represent the electrons that have been condensed into a "superfluid" state, while the rest of the electrons remains in the normal state. The fraction $\frac{n_s}{n}$ goes from zero above the T_c to unity when temperature approaches to zero. As we have discussed earlier in section 3.2, the superconducting electron density n_s drops to zero at S-N interface.

As a simple model, the two fluid model describes the electrodynamic properties of the "normal" and "superfluid" electrons in the alternating electromagnetic fields.

3.6 London Model

Meissner effect points to the importance of diamagnetic properties of the superconductors. In contrast to the two fluid model, the phenomenological theory proposed by Fritz and Hans London[30] in 1934 assuming the diamagnetic aspects are more fundamental to superconductors than the electric properties. In London model the supercurrent J_s is related to the magnetic vector potential $\vec{A}$ by

$$\vec{J}_s = -\frac{1}{\Lambda c}\vec{A}. \tag{3.14}$$

where Λ is a constant depends on material, and c is speed of light in vacuum. The divergence of $\vec{A}$ is chosen to be zero to ensure current conversation. It follows from 3.14 that a magnetic field penetrates only a thin layer of distance

$$\lambda_L = \sqrt{\Lambda c^2/4\pi} \tag{3.15}$$

through superconductor, which is refereed as London penetration depth.

Follows the Maxwell's equation, the electric and magnetic fields in a superconductor can be expressed as London Equations[25].

$$\vec{E} = \frac{4\pi\lambda^2}{c^2}\frac{\partial \vec{J}_s}{\partial t};$$

$$\vec{h} = \frac{4\pi\lambda^2}{c}\nabla \times \vec{J}_s \tag{3.16}$$

where λ is the London penetration depth, $\vec{J}_s$ is the supercurrent, and c is the speed of light in vacuum.

The London model can be used to study the vortex lattices if the diameter of a vortex core is small so that most of the volume of the sample is in superconducting phase. This condition requires that the coherence length ξ is much smaller than the penetration depth λ since the diameter of a vortex core is proportional to ξ, or, the inter-vortex spacing is larger compare to the coherence length ξ.

The average magnetic field density is then:

$$B = n\phi_0,$$ (3.17)

where n is the vortex density.

The magnetic field outside of the vortex core of radius ξ is assumed to satisfy the London equations Eqs. 3.16 which can be written as:

$$\lambda^2 \nabla^2 \vec{h}(r) + \vec{h}(r) = \vec{\Phi}_0 \delta(r)(r > \xi)$$ (3.18)

where $\vec{\phi}_0$ is parallel to the direction of vortex line. A δ function is added to satisfy the flux quantization condition, since integration of the London Equation over an area S with radius $r \gg \lambda$ surrounding the vortex line must equal Φ_0.

The London equation has an exact solution outside of the vortex core area

$$h(r) = \frac{\phi_0}{2\pi\lambda^2} K_0 \left(\frac{r}{\lambda}\right),$$ (3.19)

where $K_0 \left(\frac{r}{\lambda}\right)$ is zero order Modified Bessel Function of the second kind.

We can obtain the current density $\vec{J}$ associate with magnetic field $\vec{h}$ via the Maxwell equation

$$\nabla \times \vec{h} = \frac{4\pi}{c}\vec{J}. \tag{3.20}$$

Therefore, the supercurrent outside of the vortex core can be written as

$$J_s = \frac{\phi_0 c}{8\pi^2\lambda^3}K_1\left(\frac{r}{\lambda}\right), \tag{3.21}$$

where $K_1\left(\frac{r}{\lambda}\right)$ is the first order modified Bessel function of the second kind.

Both equations 3.19 and 3.21 diverge at the center of the vortex cores. This divergence results from the fact that the suppression of the order parameter to zero at the vortex core center is not built into the London model. There are a number ways to fix this, one is suggested by Clem[26].

In the model we are going to describe in the next chapter, we deal with non-conducting inclusions of very large core areas – their radii could be more than 1000 Å. The boundary-conditions and flux quantization require that the magnetic field inside an inclusion of given radius be constant. When the London equations are applied, the magnetic fields and super-currents are both finite inside and outside of the inclusion. Therefore, there is no divergence in our model.

The justifications of using London model in this case is given by the fact that the external magnetic field in our experiment is low and therefore the inter-vortex spacing is large; and for a non-conducting inclusion, although its diameter is large, we can use boundary conditions to determine the magnetic field inside the inclusion. In the superconducting regions the London equations can be applied.

Chapter 4

Magnetic field of isolated vortex

and inclusion

4.1 Magnetic field of an isolated vortex line which has been

trapped in a cylindrical non-conducting inclusion

If the applied magnetic field is slightly higher than the lower critical field H_{c_1}, the vortex

separation will be large enough that the interaction between vortices can be neglected, so

that we can treat each vortex as an isolated vortex line. It is interesting to know that in

the presence of cylindrical inclusions in the vicinity, will the isolated vortex line be trapped

into the inclusion or remain free? If the vortex line is trapped into the inclusion, will it be

free to move out? We will answer these questions in this section and the next. We are also

going to calculate the energy of isolated cylindrical inclusion with a vortex line trapped in

its center and the interaction between such a inclusion with a neighboring vortex.

The conducting and non-conduction cylindrical material in superconductor studied by

Mkrtchan and Shmidt[27] (1972) using image technique and by Nordborg and Vinokur[28]

32

(2000). For an infinitely long cylindrical non-conducting inclusion, the field inside the inclusion is produced by the supercurrents surrounding the boundary of the cylinder, since there are no currents inside. The situation is analogous to an infinitely long solenoid with current surrounding it. We know that the magnetic field inside the infinitely long solenoid is constant. We'll show that the magnetic field inside the infinitely long cylindrical inclusion is also constant.
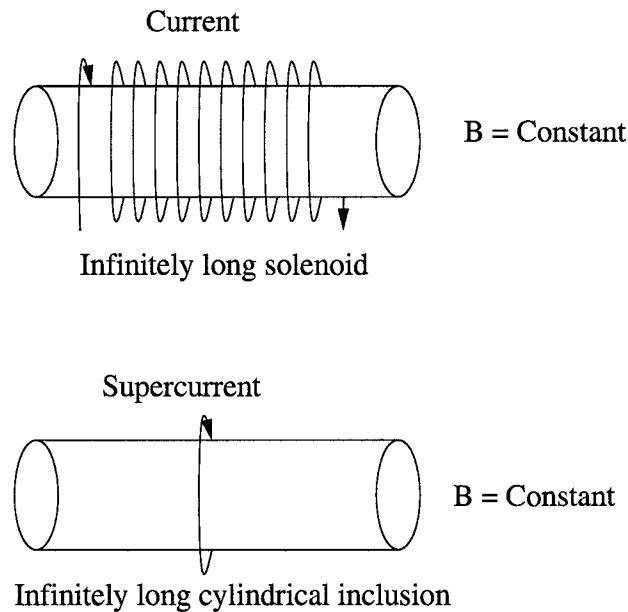
Figure 4.1: Magnetic field inside an infinitely long cylindrical non-conducting inclusion. In analogy with the internal magnetic field of the infinitely long solenoid with constant current surrounding it, we can see that the internal magnetic field of infinitely long non-conducting cylindrical inclusion with supercurrent surrounding it should be constant as well.

4.1.1 Boundary conditions

Since there is no current inside the non-conducting inclusion, the perpendicular component of current at the cylindrical boundary of the inclusion is zero. The magnetic field $h(\vec{r}, \theta)$

satisfies the homogeneous London equation,

$$\nabla^2 \vec{h}(r,\theta) + \frac{1}{\lambda^2} \vec{h}(r,\theta) = 0. \tag{4.1}$$

with boundary condition:

$$\vec{J} \cdot \hat{n}|_{r=r_0} = 0 \tag{4.2}$$

Since $(\nabla \times \vec{h}(r,\theta)) \cdot \hat{\theta} = \mu_0 \vec{J}$, the boundary condition can be written as

$$\left(\nabla \times \vec{h}(r,\theta) \cdot \hat{n} \right)_{r=r_0} = 0 \tag{4.3}$$

In cylindrical coordinate, the above boundary condition becomes

$$\left(\frac{1}{r_0} \left(\frac{\partial h_z}{\partial \theta} - \frac{\partial h_\theta}{\partial z} \right) \hat{r} + \left(\frac{\partial h_r}{\partial z} - \frac{\partial h_z}{\partial r} \right) \hat{\theta} + \left(\frac{1}{r} \frac{\partial h_\theta}{\partial r} - \frac{1}{r} \frac{\partial h_r}{\partial \theta} \right) \hat{z} \right) \cdot \hat{n}|_{r=r_0} = 0, \tag{4.4}$$

which gives

$$\left(\frac{\partial h_z}{\partial \theta} - \frac{\partial h_\theta}{\partial z} \right)_{r=r_0} = 0. \tag{4.5}$$

For an infinitely long cylindrical inclusion, there is no $\hat{z}$ dependence of $\vec{h}$, so $\frac{\partial h_\theta}{\partial z} = 0$.

Therefore,

$$\frac{\partial h_z}{\partial \theta}|_{r=r_0} = 0; \tag{4.6}$$

Which means that h_z has no θ dependence at the boundary of the cylindrical inclusion.

When r_0 is given, h_z is constant on the boundary. For an infinitely long cylindrical inclusion

along $\hat{z}$, the magnetic field inside the inclusion has only a $\hat{z}$ component from symmetry considerations, therefore, at the boundary,

$$h(r_0, \theta) = h_z(r_0) = constant. \tag{4.7}$$

Since the inclusion is non-conducting, the supercurrent $\vec{J} = 0$ for $r < r_0$, and the magnetic field inside the inclusion has only a $\hat{z}$ component, as previously stated, that gives $\frac{\partial h_z}{\partial r} = 0$ for $r < r_0$. As $h(r)$ is constant on the boundary and has no r dependence for $r < r_0$, we reached the conclusion that $h(r)$ is constant inside the inclusion.

4.1.2 The magnetic field of an isolated cylindrical inclusion with a vortex line at center

As we have mentioned at the beginning of the chapter, when the applied field is slightly higher than H_{c1}, the vortex lines are far apart from each other so that they can be treated as isolated vortex lines. In the following, we are going to show that it is energetically favorable for a vortex line to be trapped inside of a cylindrical inclusion. First, we are going to calculate the magnetic field distribution of an isolated cylindrical inclusion.

The magnetic field inside the cylindrical non-conducting inclusion is a function of the radius of the inclusion. The magnetic field outside the inclusion, in the superconducting region, satisfies homogeneous London equation:

$$\vec{h} = \vec{h}_0 \qquad (r < r_0) \tag{4.8}$$

$$\nabla^2 \vec{h}(r, \theta) + \frac{1}{\lambda^2} \vec{h}(r, \theta) = 0 \qquad (r > r_0) \tag{4.9}$$
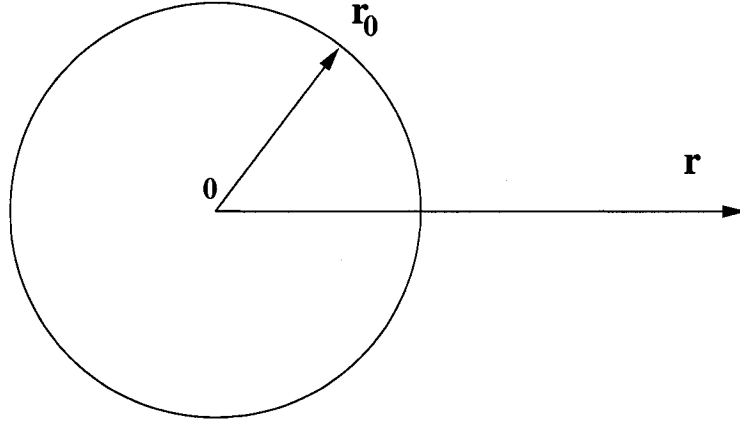
Figure 4.2: An isolated infinitely long cylindrical non-conducting inclusion with radius r_0.

where $\vec{r_0}$ is the radius of the inclusion. For an infinitely long cylindrical inclusion, the symmetry enables us to discuss the problem in 2D space.

The solution of the London equation can be written as

$$h_{in}(r) = h_0 \qquad (r < r_0) \tag{4.10}$$

$$h_{out}(r, \theta) = \sum_m A_m K_m(\frac{r}{\lambda}) e^{im\theta} \qquad (r > r_0) \tag{4.11}$$

where $\vec{h}_{in}(r)$ is the magnetic field inside the inclusion, which is a constant for a given r; $\vec{h}_{out}(r, \theta)$ is the magnetic field outside the inclusion produced by the supercurrent (outside the cylindrical surface of the inclusion), and $K_m(\frac{r}{\lambda})$ is m order Modified Bessel Function of the Second Kind.

It is convenient to define a dimensionless variable $x = \frac{r}{\lambda(0)}$, where $\lambda(0)$ is the zero degree temperature penetration depth. In units of $\lambda(0)$, the radius of the inclusion can be written as $r_0 = x_0 \lambda(0)$. We can then re-write the solution of London's equations as

$$h_{in}(x) = h_0 \qquad (x < x_0) \tag{4.12}$$

$$h_{out}(x, \theta) = \sum_m A_m K_m(x) e^{im\theta} \qquad (x > x_0) \tag{4.13}$$

with boundary condition

$$h_{out}|_{x_0} = h_{in} = h_0. \tag{4.14}$$

Applying this boundary condition we have

$$h_0 = A_0 K_0(x_0) + \sum_{m \neq 0} A_m K_m(x_0) e^{im\theta}. \tag{4.15}$$

Which gives

$$h_0 = A_0 K_0(x_0) \qquad m = 0; \tag{4.16}$$

$$0 = \sum_{m \neq 0} A_m K_m(x_0) e^{im\theta} \qquad m \neq 0. \tag{4.17}$$

where $K_0(\frac{r}{\lambda})$ is zero order Modified Bessel Function of the Second Kind.

Solving the above equations, we get A_0 and A_m:

$$A_0 = \frac{h_0}{K_0(x_0)}; \tag{4.18}$$

$$A_m = 0. \tag{4.19}$$

The magnetic field outside of the inclusion(superconducting region) can then be written

as

$$h_{out}(x) = \frac{h_0}{K_0(x_0)} K_0(x) \qquad (x > x_0). \tag{4.20}$$

Here, h_0 is the magnetic field inside the inclusion, which is a constant for a given r_0. Its value will be determined by using the fluxoid quantization condition.

F. London [30] introduced the concept of the flux quantum and flux quantization to describe the mixture of normal and superconducting domains. For a normal domain in the type-II superconductor, the fluxoid Φ' equals the ordinary magnetic flux through the non-superconducting region plus magnetic flux induced by supercurrents via any contour integration enclosing the non-superconducting region. It can be written as

$$\Phi' = \Phi + \oint \lambda^2 \vec{J_s} \cdot d\vec{l}, \tag{4.21}$$

where $\Phi = \int \vec{h} \cdot d\vec{S}$ is the magnetic flux through the non-superconducting region. The fluxoid quantization condition states that fluxoid Φ' can only have integral multiples of a fluxoid quantum Φ_0,

$$\Phi' = n\Phi_0, \tag{4.22}$$

where

$$\Phi_0 = \frac{hc}{2e} = 2.07 \times 10^{-15} Wb \tag{4.23}$$

is the fluxoid quantum constant. The path integral in equation can be any closed path surrounding the non-superconducting area. Normally it is convenient take this just outside the non-superconducting region.

Applying the fluxoid quantization condition to the cylindrical non-conducting inclusion, we have

$$\Phi + \lambda^2 \oint (\nabla \times \vec{h}) \cdot \vec{dl} = n\Phi_0. \tag{4.24}$$

In polar coordinate, the fluxoid quantization condition becomes

$$\Phi + \lambda^2 \oint r_0 (-\frac{\partial h}{\partial r}) d\theta = n\Phi_0. \tag{4.25}$$

By inserting h_{out} into the above equation, and using a contour that just encloses the non-superconducting region, we can then determine the value of h_0

$$\pi r_0^2 h_0 - \lambda^2 x_0 \oint \frac{h_0}{K_0(x_0)} K_0'(x_0) = n\Phi_0. \tag{4.26}$$

Using relation $K_0'(x) = -K_1(x)$, we have

$$h_0 = \frac{\Phi_0}{2\pi\lambda^2 x_0} \frac{n K_0(x_0)}{K_1(x_0) + \frac{x_0}{2} K_0(x_0)}. \tag{4.27}$$

h_0 is the magnetic field inside the inclusion area, which is a constant for a given inclusion radius.

Outside the inclusion, the magnetic field is

$$h_{out} = \frac{\Phi_0}{2\pi\lambda^2 x_0} \frac{n K_0(x)}{K_1(x_0) + \frac{x_0}{2} K_0(x_0)}, \tag{4.28}$$

where $x = \frac{r}{\lambda(0)}$ is the distance from a field point to the center of the inclusion.

We see here that the magnetic fields inside and outside of the inclusion have finite values; there is no divergence in our model.

4.1.3   Magnetic field energy of an isolated cylindrical inclusion with a vortex line at its center

The magnetic field energy per unit length of a cylindrical inclusion with a vortex line at its center consists of the magnetic field energy of the inclusion and the contributions from outside of the inclusion (which include magnetic field energy in the superconducting region and the kinetic energy of the currents).

$$
\begin{aligned}
E &= \frac{1}{8\pi} \int_{r<r_0} h_0^2 dS + \int \left(\frac{h^2}{8\pi} + \frac{1}{2} m v_s^2 n_s \right) dS \\
&= \frac{1}{8} r_0^2 h_0^2 + \frac{1}{8\pi} \int_{r>r_0} \left(h^2 + \lambda^2 (\nabla \times h)^2 \right) dS.
\end{aligned}
\tag{4.29}
$$

The first term is the contribution from the inclusion core, and the second term

$$
E_1 = \frac{1}{8\pi} \int_{r>r_0} \left(h^2 + \lambda^2 (\nabla \times h)^2 \right) dS,
\tag{4.30}
$$

is the contribution from superconducting region. From the London equation

$$
\vec{h} + \lambda^2 \nabla \times \nabla \times \vec{h} = \vec{\Phi}_0 \delta_2(r_1, 0),
\tag{4.31}
$$

we have

$$
\begin{aligned}
E_1 &= \frac{1}{8\pi} \int_{r>r_0} \left(h^2 + \lambda^2 (\nabla \times h)^2) \right) dS \\
&= \frac{1}{8\pi} \int \left(\vec{h} + \lambda^2 \nabla \times \nabla \times \vec{h} \right) \cdot \vec{h} dS + \frac{\lambda^2}{8\pi} \oint \left(\vec{h} \times (\nabla \times \vec{h}) \right) \cdot d\vec{S} \\
&= \frac{1}{8\pi} \int_{r>r_0} \Phi_0 h \delta_2(r_1, 0) dS + \frac{\lambda^2}{8\pi} \oint \left(\vec{h} \times (\nabla \times \vec{h})^2 \right) \cdot d\vec{S}.
\end{aligned}
\tag{4.32}
$$

For an isolated inclusion, the first term vanishes. The surface integral is taken along the inner(cylindrical surface of inclusion) and the outer boundaries of the integration area. Since the outer boundary goes to infinity, the surface integral at the outer boundary makes no contribution. The inner boundary is chosen along the border of the cylindrical inclusion. Note that $d\vec{S}$ here is pointed to the center of the inclusion. We have

$$
\begin{aligned}
E_1 &= \frac{\lambda^2}{8\pi} \int \vec{h} \times (\nabla \times h) \cdot d\vec{S} \\
&= -\frac{\lambda^2}{8\pi} \oint_{r=r_0} r_0 h \frac{\partial h}{\partial r} d\theta = \frac{\lambda^2 h_0^2 x_0}{4} \frac{K_1(x_0)}{K_0(x_0)},
\end{aligned}
\tag{4.33}
$$

where $x_0 = \frac{r_0}{\lambda(0)}$.

Finally, the total energy of an isolated inclusion with a vortex line at it center is

$$
\begin{aligned}
E &= \frac{1}{8} r_0^2 h_0^2 + \frac{\lambda^2 h_0^2 x_0}{4} \frac{K_1(x_0)}{K_0(x_0)} \\
&= \frac{n^2 \Phi_0^2}{16\pi^2 \lambda^2} \frac{K_0(x_0)^2}{x_0 K_0(x_0) \left(K_1(x_0) + \frac{x_0}{2} K_0(x_0)\right)}.
\end{aligned}
\tag{4.34}
$$

For comparison, we are going to calculate the magnetic energy of an isolated normal vortex line. The magnetic field of an isolated vortex line is given by

$$
h(r) = \frac{\phi_0}{2\pi\lambda^2} K_0 \left(\frac{r}{\lambda}\right).
\tag{4.35}
$$

Following the steps similar to above, we can show that the energy of an isolated vortex line is similar to that of an isolated inclusion, except that for a vortex line, the contribution from the vortex core can be neglected. The only contribution to the integral is from the vortex core boundary,

$$E = \frac{\lambda^2}{8\pi} \oint (h \times (\nabla \times h)) \cdot d\vec{S} = -\frac{\lambda^2}{8\pi} \left(2\pi r h(r) \frac{\partial h}{\partial r} \right)_{r=\xi}, \tag{4.36}$$

where ξ is the coherence length. For $\xi < r \ll \lambda$, the energy can be written as

$$E = \frac{\phi_0^2}{16\pi^2 \lambda^2} ln\left(\frac{\lambda}{\xi}\right). \tag{4.37}$$
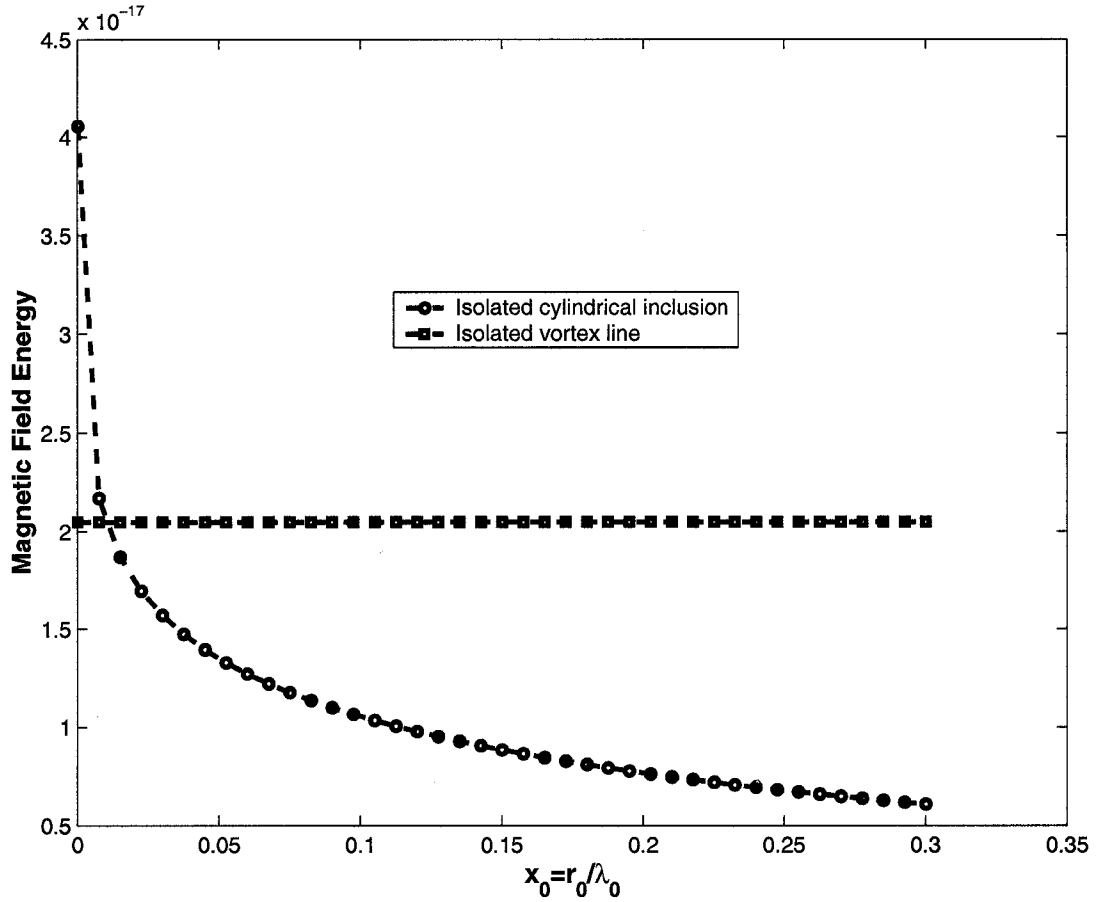
Figure 4.3: Energies(relative value) of an isolated vortex line with $x_0 = \frac{\xi}{\lambda(0)} = 0.01$ (solid line) and an isolated cylindrical inclusion with $x_0 = \frac{r_0}{\lambda(0)}$ as functions of x_0, where r_0 is the radius of the inclusion. For $x_0 > \xi$, the energy of isolated cylindrical inclusion is lower than that of isolated vortex line.

Fig. 4.3 shows the total energy of an isolated cylindrical inclusion(with one flux quantum trapped in its center) as function of $x_0 = \frac{r_0}{\lambda(0)}$. For comparison, the energy of an isolated vortex line with $\xi = 14$ Å is also shown as function of $x_0 = \frac{\xi}{\lambda(0)}$. The energy of an isolated vortex line is constant for a given ξ, see Eq.4.37. One can see that for $x_0 \geq \xi$, the energy of an isolated cylindrical inclusion is lower than that of an isolated vortex line. This indicates that it is energetically favorable for an isolated vortex line to be trapped into an nearby inclusion.

For $r_0 \leq \xi$, we let both r_0 and ξ vary, see Fig. 4.4 where we compare the total energy of an isolated vortex line with that of an isolated cylindrical inclusion of small radius with one flux quantum in its center. When the radius of the inclusion is very small, the total energy of an isolated inclusion should approach the total energy of an isolated normal vortex line. We see in Fig. 4.4 that in the range x_0 from 0.001 to 0.01, which corresponds to ξ range from 1.4 Å to 14 Å, there is good agreement in total energy between an isolated cylindrical inclusion and an isolated vortex line. In many practical applications of high-T_C superconducting materials, column defects are introduced to create strong pinning in order to pin the vortices even when strong currents exert strong forces transverse to the vortex axis. To effectively capture the vortex lines, the radii of theses column defects should be large enough so that the energy of a column defect with a vortex line trapped in it is lower that the energy of an isolated vortex line.

It is energetically favorable for an isolated vortex line to be trapped into inclusions of larger radii. For inclusions of small radii(up to 10 ξ for YBCO), the energy of an isolated vortex line is similar to that of an isolated inclusion with a vortex line trapped in its center.
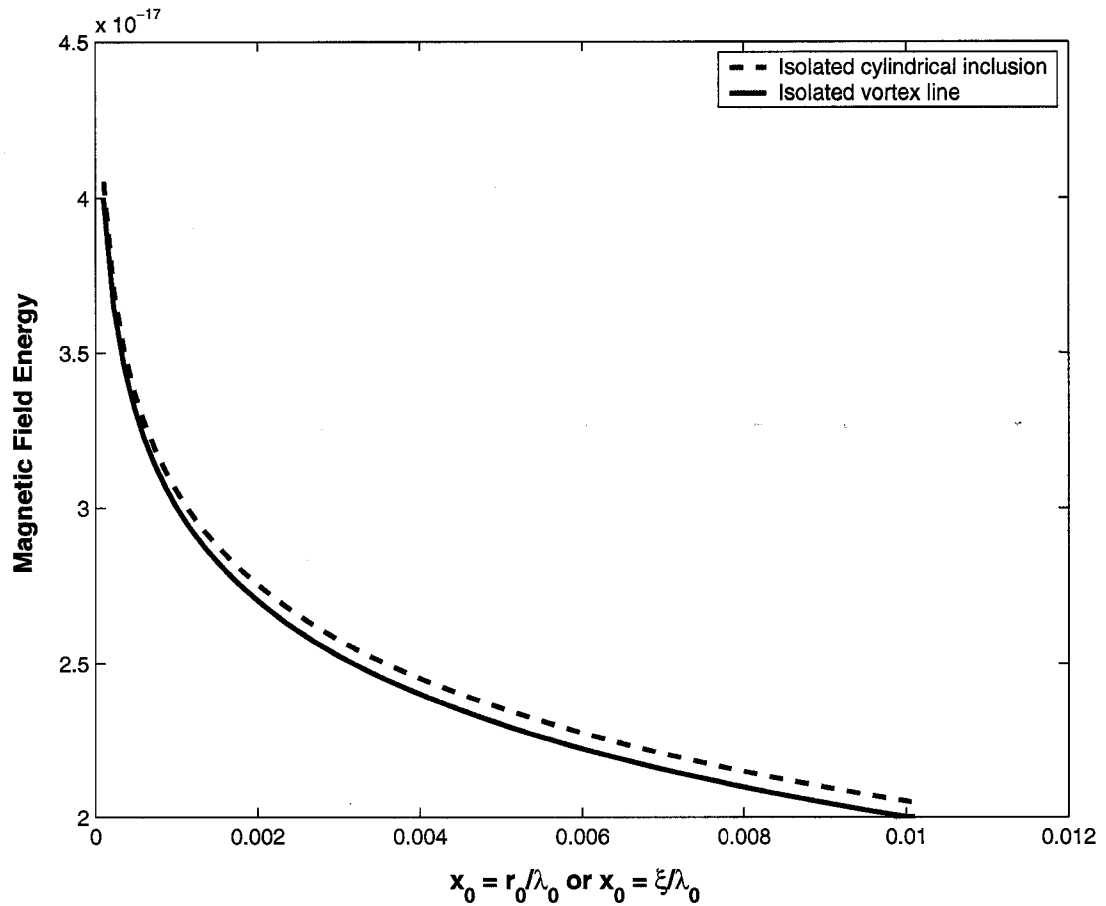
Figure 4.4: Energies(relative value) of isolated vortex line as function of $x_0 = \frac{\xi}{\lambda(0)}$ compares with energies of isolated cylindrical inclusion as function of $x_0 = \frac{r_0}{\lambda(0)}$. For very small x_0 they are identical.

4.2   Interaction between a cylindrical inclusion and one neighbor vortex

4.2.1   Magnetic field

In this section we discuss the magnetic field distribution of a cylindrical non-conducting inclusion with a single neighboring vortex. From now on, when we talk about an inclusion, by default there is a vortex line trapped in it. We also discuss the interaction energy between

the inclusion and a neighboring vortex. For the same reason as was discussed in 4.1.1, the

magnetic field inside the inclusion has a constant value which depends on the radius of the

inclusion. However, the field in the superconducting region now has contributions from the

supercurrents surrounding the inclusion as well as from the neighbor vortex located at r_1,

Fig.4.5.
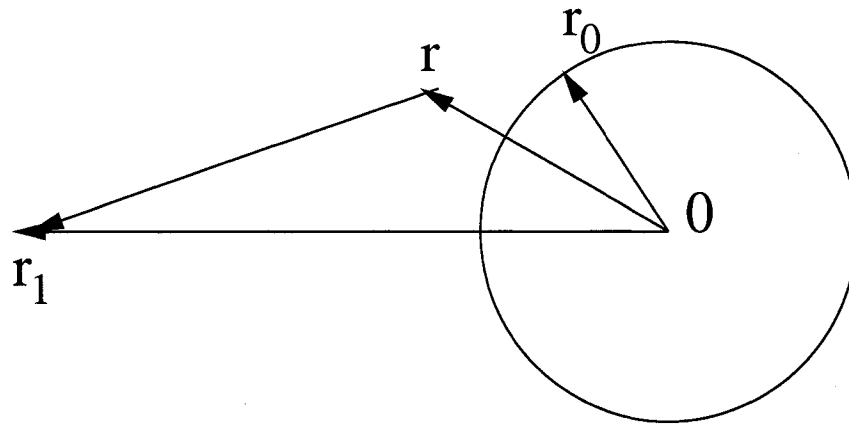
Figure 4.5: Infinitely long cylindrical non-conducting inclusion of radius r_0 with one neighbor vortex located at r_1.

The magnetic field outside the inclusion satisfies the London equation

$$\nabla^2 \vec{h}(r,\theta) + \frac{1}{\lambda^2}\vec{h}(r,\theta) = \frac{\vec{\Phi}_0}{\lambda^2}\delta(r_1). \qquad (r > r_0) \tag{4.38}$$

If we limit our discussion to the superconducting region between the inclusion and its

neighbor vortex, i.e. $r_0 < r < r_1$, then this equation is homogeneous. The solution inside

and outside of the inclusion can be written as:

$$h_{in}(r) = h_0 \qquad (r < r_0); \tag{4.39}$$

$$h_{out}(r, \theta) = \sum_m A_m K_m(\frac{r}{\lambda}) e^{im\theta} \qquad (r > r_0); \tag{4.40}$$

$$h_{vortex}(r, \theta) = \frac{\Phi_0}{2\pi\lambda^2} K_0 \left(\frac{|\vec{r_1} - \vec{r}|}{\lambda} \right)$$

$$= \frac{\Phi_0}{2\pi\lambda^2} \sum_m I_m \left(\frac{r}{\lambda} \right) K_m \left(\frac{r_1}{\lambda} \right) e^{im\theta} \qquad (r_0 < r < r_1). \tag{4.41}$$

Here, $\vec{h}_{in}(r)$ is the constant magnetic field inside the inclusion of radius r_0; $\vec{h}_{out}(r, \theta)$ is

the magnetic field outside the inclusion due to the supercurrent surrounding the boundary

of inclusion produced by the flux quanta trapped in the inclusion, and, $\vec{h}_{vortex}(r, \theta)$ is the

magnetic field produced by the vortex located at $\vec{r_1}$. $K_m(\frac{r}{\lambda})$ is m order Modified Bessel

Function of the Second Kind and $I_m(\frac{r}{\lambda})$ is m order Modified Bessel Function of the First

Kind.

The magnetic field in the superconducting region between r_0 and r_1 is the superposition

of $\vec{h}_{out}(r, \theta)$ and $\vec{h}_{vortex}(r, \theta)$,

$$\vec{h}_{sc}(r, \theta) = \vec{h}_{out}(r, \theta) + \vec{h}_{vortex}(r, \theta) \qquad (r_0 < r < r_1). \tag{4.42}$$

With $x_0 = r_0/\lambda(0)$, $x = r/\lambda(0)$ and $x_1 = r_1/\lambda(0)$, we have

$$h_{in}(x) = h_0 \qquad (x < x_0); \tag{4.43}$$

$$h_{out}(x, \theta) = \sum_m A_m K_m(x) e^{im\theta} \qquad (x > x_0); \tag{4.44}$$

$$h_{vortex}(x, \theta) = \frac{\Phi_0}{2\pi\lambda^2} \sum_m I_m(x) K_m(x_1) e^{im\theta} \qquad (x_0 < x < x_1); \tag{4.45}$$

$$h_{sc}(x, \theta) =$$

$$\sum_m \left(A_m K_m(x) + \frac{\Phi_0}{2\pi\lambda^2} I_m(x) K_m(x_1) e^{im\theta} \right) \qquad (x_0 < x < x_1), \tag{4.46}$$

with the boundary condition

$$\vec{h}_{sc}|_{x_0} = \vec{h}_{in} = \vec{h}_0. \tag{4.47}$$

A_0 and A_m can be determined by applying the above boundary condition.

$$A_0 = \frac{1}{K_0(x_0)} \left(h_0 - \frac{\Phi_0}{2\pi\lambda^2} I_0(x_0) K_0(x_1) \right) \qquad m = 0; \tag{4.48}$$

$$A_m = \frac{-1}{K_m(x_0)} \frac{\Phi_0}{2\pi\lambda^2} I_m(x_0) K_m(x_1) \qquad m \neq 0. \tag{4.49}$$

The magnetic field in the superconducting region can be written as

$$h_{sc}(x) = \frac{h_0 K_0(x)}{K_0(x_0)}$$

$$+ \frac{\Phi_0}{2\pi\lambda^2} \sum_m \frac{K_m(x_1)}{K_m(x_0)} \left(-I_m(x_0) K_m(x) + K_m(x_0) I_m(x) \right) e^{im\theta}, \tag{4.50}$$

where h_0 is the magnetic field inside the inclusion. Although it is a constant, its value yet

to be determined. The sum of m goes from $-\infty$ to $+\infty$.

Next, we will use the fluxoid quantization condition to determine h_0. In 2D polar coordinates, the fluxoid quantization can be written as

$$\Phi + \lambda^2 \oint r_0(-\frac{\partial h}{\partial r})d\theta = n\Phi_0. \tag{4.51}$$

Inserting h_{sc} into the above fluxoid quantization condition, one can determine h_0. Using a contour that just encloses the non-superconducting region (along the border of the cylindrical inclusion), we get

$$\pi r_0^2 h_0 - \lambda^2 r_0 \oint \frac{h_0}{\lambda K_0(x_0)} K_0'(x_0)$$

$$- \lambda^2 r_0 \oint \frac{\Phi_0}{2\pi\lambda^2} \sum_m \frac{1}{\lambda} \left(I_m'(x_0)K_m(x_1) - \frac{I_m(x_0)K_m(x_1)}{K_m(x_0)} K_m'(x_0) \right) e^{im\theta}d\theta$$

$$= n\Phi_0. \tag{4.52}$$

Since $\oint e^{im\theta}d\theta = 0$, for $m \neq 0$, carrying out the integration over θ, we get:

$$\pi r_0^2 h_0 - 2\pi\lambda^2 x_0$$

$$\left(\frac{h_0}{\lambda K_0(x_0)} K_0'(x_0) + \frac{\Phi_0}{2\pi\lambda^2} \left(I_0'(x_0)K_0(x_1) - \frac{I_0(x_0)K_0(x_1)}{K_0(x_0)} K_0'(x_0) \right) \right)$$

$$= n\Phi_0. \tag{4.53}$$

Solving the above equation we get the expression for h_0:

$$h_0 = \frac{\Phi_0}{2\pi\lambda^2 x_0} \frac{nK_0(x_0) + K_0(x_1)}{K_1(x_0) + \frac{x_0}{2}K_0(x_0)}. \tag{4.54}$$

This expression is similar to that for an isolated inclusion except that now the neighboring vortex at location r_1 also contributes a term $K_0(x_1)$ to the magnetic field inside the inclusion.
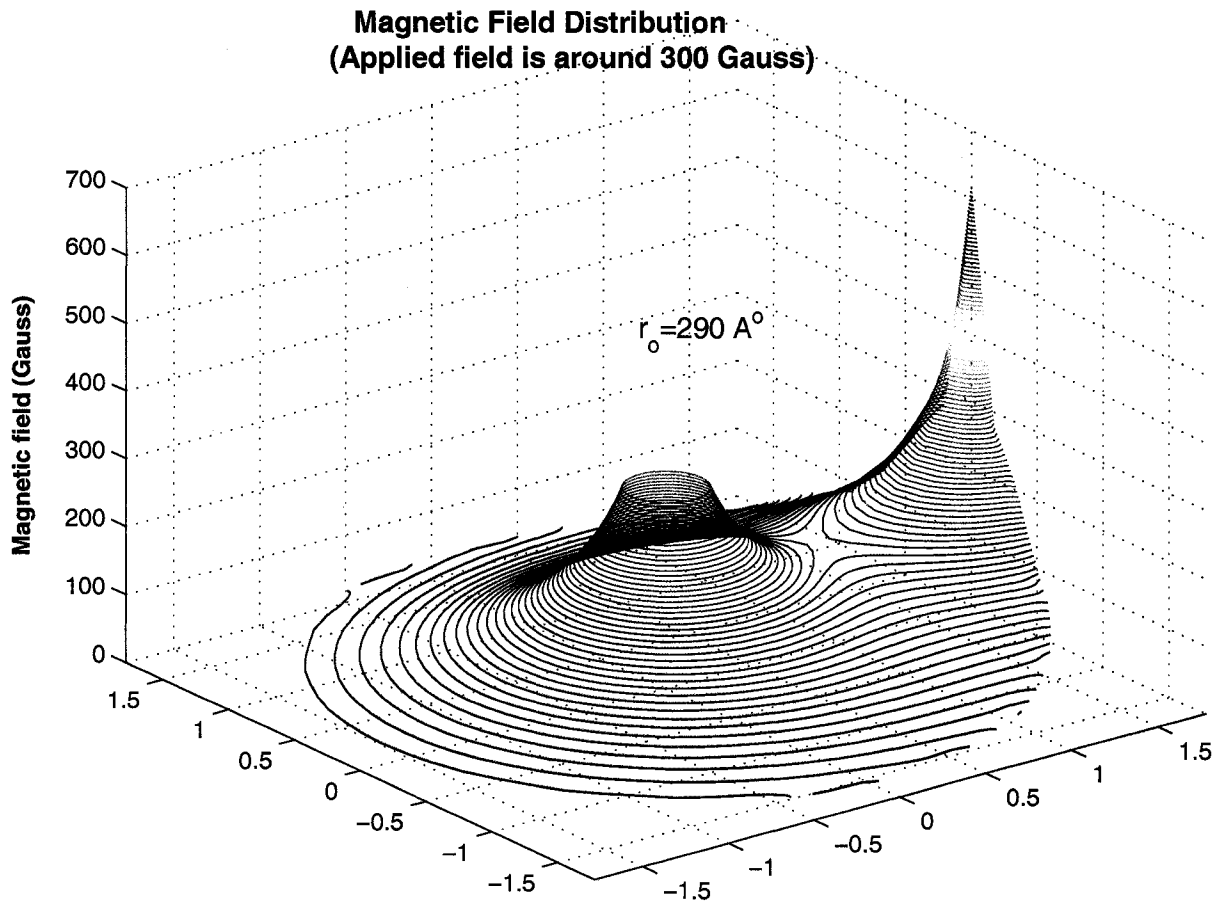
Figure 4.6: 3D Magnetic field(Gauss) distribution of an inclusion-vortex system. The Penetration depth is chosen to be 1450 $\mathring{A}$, the applied field is 300 Gauss.

Fig. 4.6 shows the 3D magnetic field distribution of an inclusion-vortex system. The dimensionless radius of the inclusion is $x_0 = r_0/\lambda_0 = 0.2$ and the normal vortex is located at $x_1 = r_1/\lambda_0 = 1.78$. The value of the vortex separation r_1 is determined by applied field which is higher than the lower critical field H_{c1} of $YBa_2Cu_3O_{7-\delta}$.
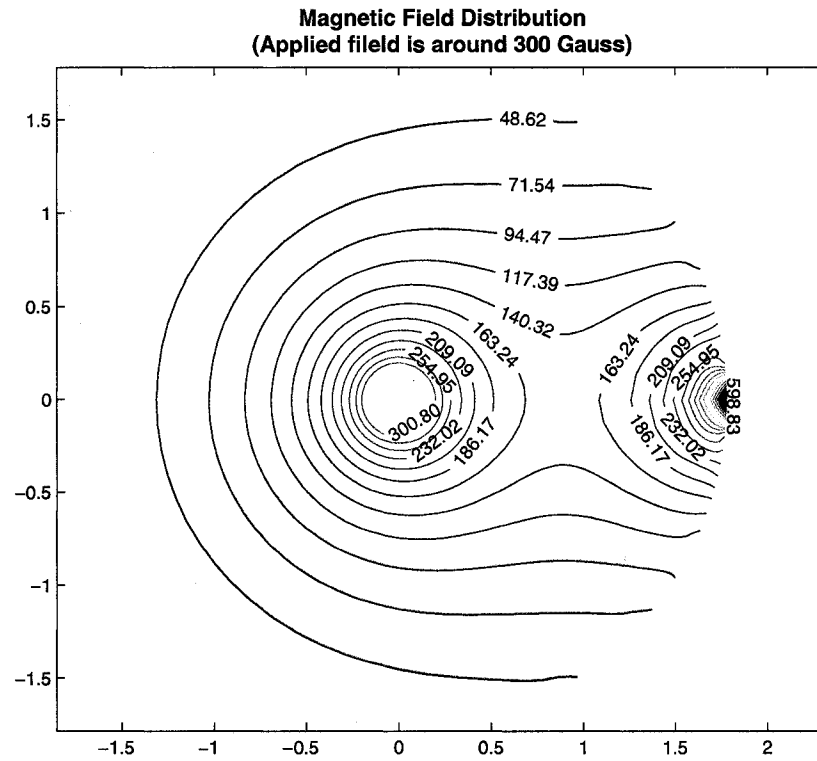
Figure 4.7: Contour plot of Magnetic field distribution of an inclusion-vortex system. The applied field is 300 Gauss, and the penetration depth is chosen to be 1450 $\overset{\circ}{A}$.

Fig.4.7 shows the contour plot corresponding to Fig.4.6. Along the line between the center of the inclusion and its neighbor vortex, the saddle point can be clearly seen.

We can further investigate the properties of the saddle point by setting $\theta = 0$ in Eq.4.50. The magnetic fields between inclusions of various radii and a normal vortex located at a fixed point r_1 are plotted in Fig.4.8. The minimum field corresponds to the saddle point.

When the vortex separation is fixed, we can see from Fig.4.8 that the saddle point position is not sensitive to the changing of the inclusion radius. This result is a little surprising – we would expect that when the radius of the inclusion increases the saddle point would be pushed further away from the center of the inclusion. This can be understood as
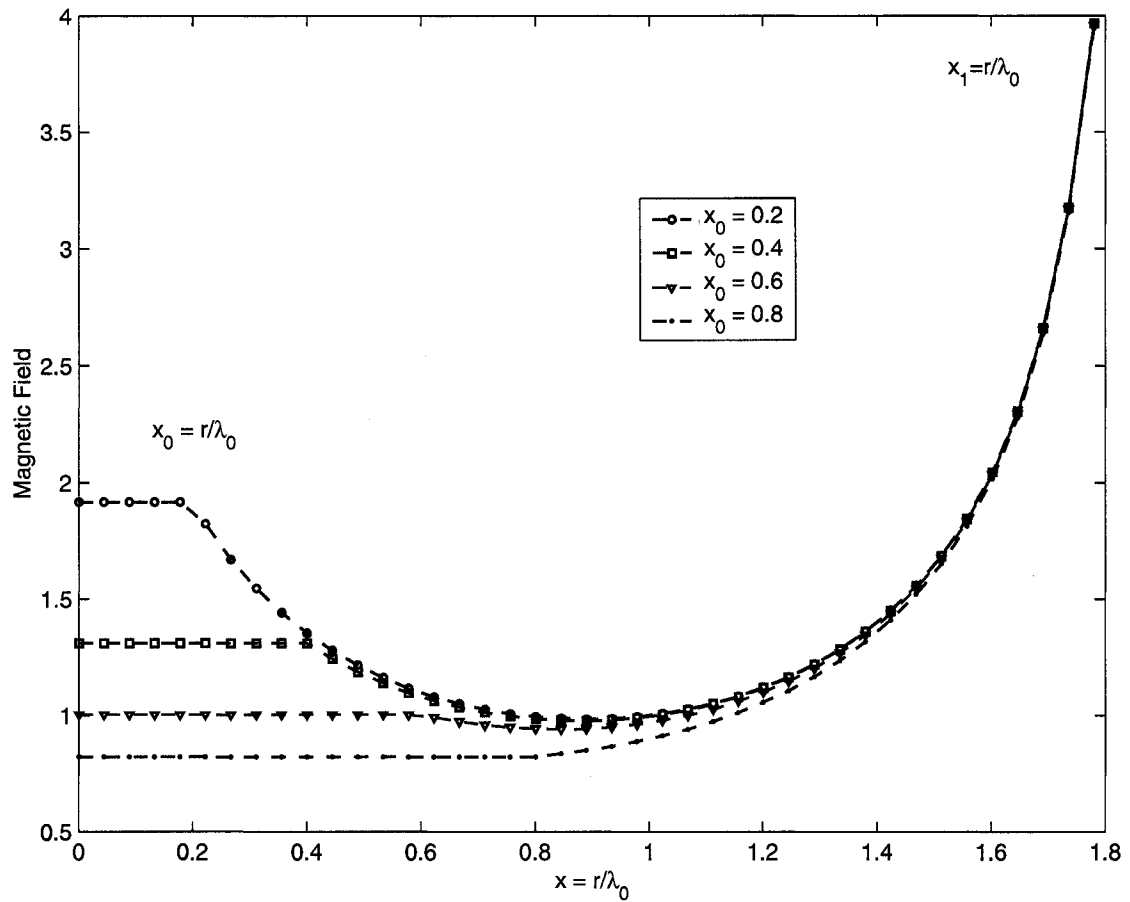
Figure 4.8: Magnetic field(relative value) in the superconducting regions as function of $x = \frac{r}{\lambda(0)}$. The minimum field corresponding to the saddle point field. Inclusions of several radii($x_0 = r_0/\lambda(0)$) values are shown.

follows. The constant field inside the inclusion is higher than the field in the superconducting regions except for points close to the vortex core located at r_1. The inclusions that have smaller radii have higher internal field than those that have larger radii. The average internal field is the weighted average of the field inside inclusions and the field in the superconducting regions.

$$h_{ave} = w_1 h_{in} + w_2 h_{sc} \qquad (4.55)$$

where $w_1 = \frac{r_0^2}{r_s^2}$, and $w_2 = \frac{r_s^2 - r_0^2}{r_s^2}$ are weights, and r_s is the distance from the center of the inclusion to the saddle point. Applying the fluxoid quantization condition, we have

$$\pi(r_s^2 - r_0^2)h_{sc} + \pi r_0^2 h_{in} = n\Phi_0. \tag{4.56}$$

If we combine with Eq.4.55, the average field can be written as

$$h_{ave} = \frac{\phi_0}{\pi r_s^2}. \tag{4.57}$$

The average field depends on r_s. If the changing of the inclusion size does not change the average field significantly, the saddle point position will remain at the same place.

4.2.2   Magnetic field energy of a cylindrical inclusion with one normal vortex neighbor

Early in Chapter 3.1.3 we found the energy of an isolated cylindrical inclusion with a vortex at its center. Here, we will extend that development and find the energy of an inclusion/normal vortex system.

When an inclusion is placed next to a vortex, the magnetic field energy per unit length of a cylindrical inclusion includes the magnetic field energy of the inclusion, the magnetic field energy in the superconducting region and the kinetic energy of the currents. This energy can be expressed as:

$$E = \frac{1}{8\pi} \int_{r<r_0} h_0^2 dS + \int \left(\frac{h^2}{8\pi} + \frac{1}{2} m v_s^2 n_s \right) dS$$

$$= \frac{1}{8} r_0^2 h_0^2 + \frac{1}{8\pi} \int_{r>r_0} \left(h^2 + \lambda^2 (\nabla \times h)^2 \right) dS. \tag{4.58}$$

Here $h(r)$ is the magnetic field in the superconducting region that includes contributions from the neighbor vortex and the supercurrents surrounding the inclusion. The first integral gives the magnetic field energy inside the inclusion. The integration area of second integral includes the normal vortex located at r_1. Using the London equation, the second and third integrals give:

$$E_1 = \frac{1}{8\pi} \int_{r>r_0} \left(h^2 + \lambda^2 (\nabla \times h)^2 \right) dS$$

$$= \frac{1}{8\pi} \int \left(\vec{h} + \lambda^2 \nabla \times \nabla \times \vec{h} \right) \cdot \vec{h} dS + \frac{\lambda^2}{8\pi} \oint \left(\vec{h} \times (\nabla \times \vec{h}) \right) \cdot d\vec{S}$$

$$= \frac{1}{8\pi} \int_{r>r_0} \Phi_0 h \delta_2(r_1, 0) dS + \frac{\lambda^2}{8\pi} \oint \left(\vec{h} \times (\nabla \times \vec{h}) \right) \cdot d\vec{S}. \tag{4.59}$$

The first integral in the above equation is integrated over an area S that includes vortices at (x_i, θ_i); doing so with the help of Eq.4.50 gives:

$$\frac{1}{8\pi} \int_{r>r_0} \Phi_0 h(x_1, \theta) \delta_2(x_1, 0) dS$$

$$= \frac{\Phi_0 h_0}{8\pi} \frac{K_0(x_1)}{K_0(x_0)}$$

$$+ \frac{\Phi_0^2}{16\pi^2 \lambda^2} \sum_m \frac{K_m(x_1)}{K_m(x_0)} \left(-I_m(x_0) K_m(x_1) + K_m(x_0) I_m(x_1) \right). \tag{4.60}$$

The surface integral is taken along the inner(cylindrical surface of the inclusion) and the outer boundary of the integration area. Since the outer boundary goes to infinity, the surface integral at the outer boundary gives no contribution. The inner boundary is along the border of cylindrical inclusion, note that $d\vec{S}$ here is pointed to the center of inclusion.

In polar coordinates with $h = h_{sc}$, the second integral gives

$$\frac{\lambda^2}{8\pi} \oint_{r=r_0} r_0 h \frac{\partial h}{\partial r} d\theta$$

$$= -\frac{\lambda^2}{8\pi} x_0 h_0 \oint \frac{h_0 K_1(x_0)}{K_0(x_0)} d\theta$$

$$+ \frac{\lambda^2}{8\pi} x_0 h_0 \frac{\Phi_0}{2\pi\lambda^2} \oint d\theta e^{im\theta} \sum_m \left(-\frac{I_m(x_0)K_m(x_1)}{K_m(x_0)} K_m(x_0)' + K_m(x_1)I_m(x_0)' \right).$$

(4.61)

Since for $m \neq 0$, $\int_0^{2\pi} e^{im\theta} d\theta = 0$, we have

$$\frac{\lambda^2}{8\pi} \oint_{r=r_0} r_0 h \frac{\partial h}{\partial r} d\theta$$

$$= -\frac{\lambda^2 x_0 h_0^2 K_1(x_0)}{4 K_0(x_0)} + \frac{x_0 h_0 \Phi_0}{8\pi} \left(\frac{I_0(x_0)K_0(x_1)}{K_0(x_0)} K_1(x_0) + K_0(x_1)I_0(x_0) \right)$$

$$= -\frac{\lambda^2 x_0 h_0^2 K_1(x_0)}{4 K_0(x_0)} + \frac{h_0 \Phi_0}{8\pi} \frac{K_0(x_1)}{K_0(x_0)}.$$

(4.62)

The magnetic field energy in the superconducting region can be written as

$$E_1 = \frac{1}{8\pi}\Phi_0 h(r_1) - \frac{\lambda^2}{8\pi}\oint_{r=r_0} r_0 h \frac{\partial h}{\partial r} d\theta$$

$$= \frac{\lambda^2 x_0 h_0^2 K_1(x_0)}{4K_0(x_0)}$$

$$+ \frac{\Phi_0^2}{16\pi^2\lambda^2}\sum_m \frac{K_m(x_1)}{K_m(x_0)}\left(-I_m(x_0)K_m(x_1) + K_m(x_0)I_m(x_1)\right). \tag{4.63}$$

The total magnetic energy of an inclusion with one neighbor vortex is

$$E = \frac{\Phi_0^2}{16\pi^2\lambda^2}\frac{(nK_0(x_0) + K_0(x_1))^2}{x_0 K_0(x_0)\left(K_1(x_0) + \frac{x_0}{2}K_0(x_0)\right)}$$

$$+ \frac{\Phi_0^2}{16\pi^2\lambda^2}\sum_m \frac{K_m(x_1)}{K_m(x_0)}\left(-I_m(x_0)K_m(x_1) + K_m(x_0)I_m(x_1)\right). \tag{4.64}$$

The sum of m goes from $-\infty$ to $+\infty$.

Fig. 4.9 shows the total energy of an inclusion - vortex system; several radii of inclusions are shown. The energy is plotted as a function of vortex separation for a given inclusion radius. When a vortex line approaches an inclusion, the interaction energy increases. When x_1 becomes less than x_0, where the figure indicates a maximum of energy, the calculation is no longer physically meaningful, though formally possible.
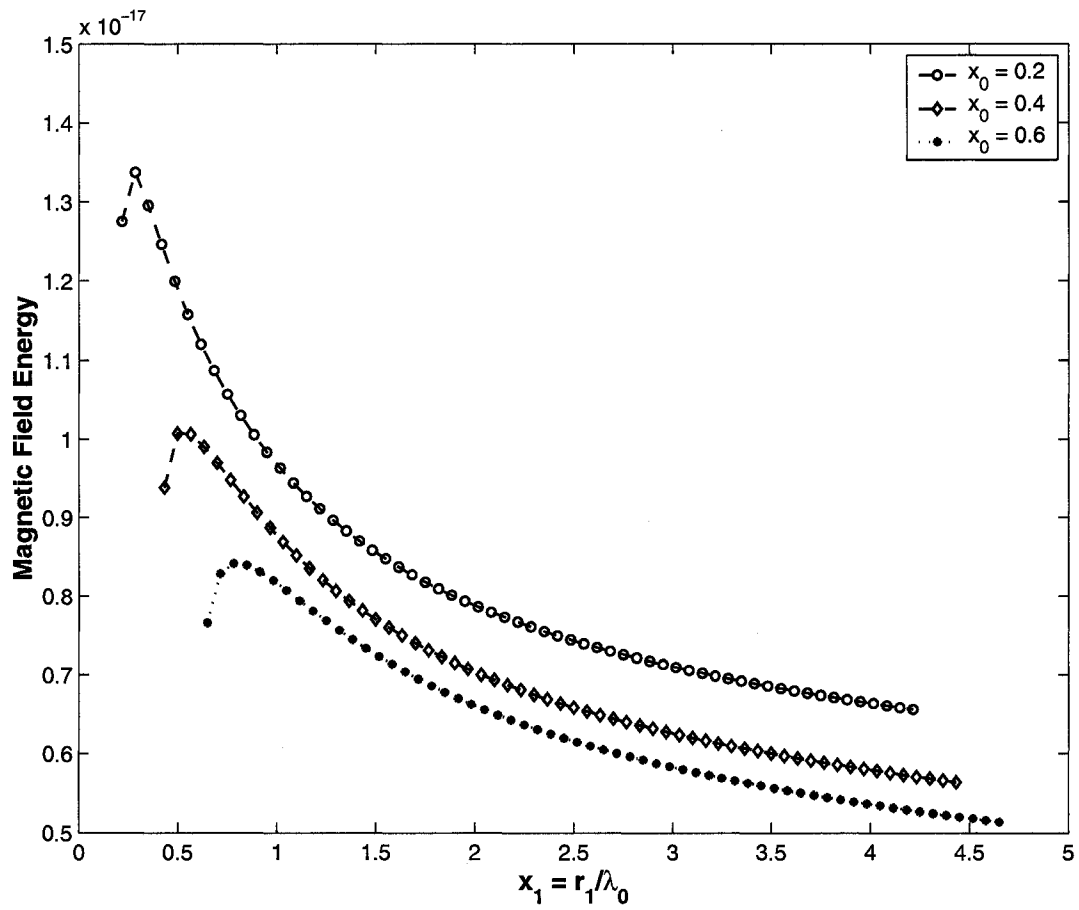
Figure 4.9: Total energy(relative value) of inclusion - vortex system. Several inclusion radii are shown. For a given inclusion radius, the energy is plotted as function of vortex separation x_1.

4.2.3   Interaction force between an inclusion and a vortex

The force between an inclusion and a vortex can be directly obtained from the interaction energy. Using Eq.4.64, the force that a vortex at r_1 feel due to the interaction with the inclusion at r_0 is

$$F = -\frac{\partial E}{\partial r_1},$$ (4.65)

where E is the total magnetic field energy of inclusion - vortex system as in Eq.4.64. If the inclusion is replaced by a vortex, we get the force between two vortices.

In experiments, the vortex spacing x_1 is fixed by the applied field. The force experienced by a vortex at x_1 of an inclusion-vortex system is plotted as function of inclusion radius x_0 in Fig.4.10.

For a given vortex separation, the repulsive force experienced by a vortex decreases as the radius of the inclusion increases. Larger inclusions have less repulsive force on the vortices near by. In another words, vortices are easier to move into inclusions with larger radii.

The force experienced by a vortex for a given inclusion radius as a function of vortex separation is shown in Fig.4.11.

When a vortex approaches an inclusion from a distance, the repulsive force increases. For a vortex to be trapped into an inclusion that already has a flux quantum in the center, it must overcome a force barrier. This force barrier decreases as the radius of the inclusion increases. Therefore, for a large inclusion it is easier to have another vortex trapped into it than for smaller inclusions. But on the other hand, inclusions with smaller radii will hold
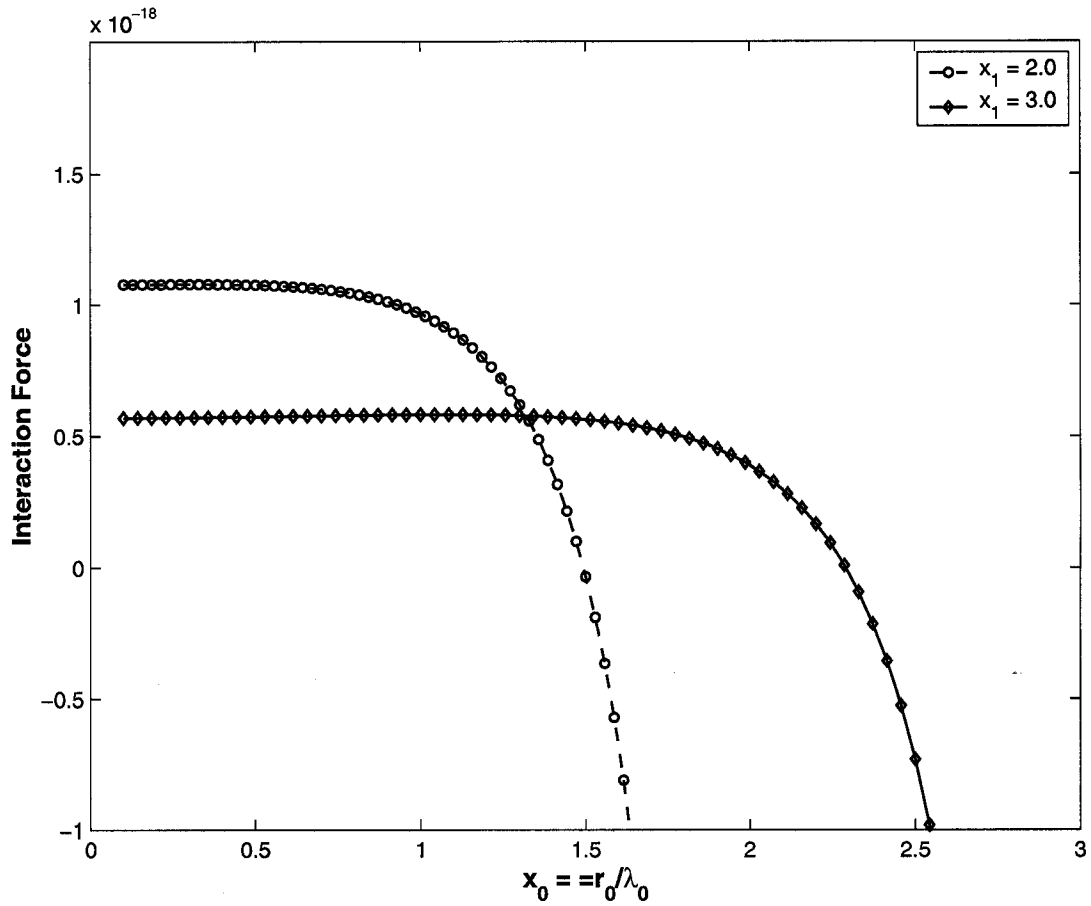
Figure 4.10: Interaction forces(relative value) between an infinitely long cylindrical non-conducting inclusion and a neighbor vortex. For fixed vortex separation r_1, the force experienced by vortex located at $x_1 = \frac{r_1}{\lambda(0)}$ is plotted as function as inclusion radius $x_0 = \frac{r_0}{\lambda(0)}$. The interaction force decreases for large inclusions.

flux quanta tighter once trapped in, since the flux vortex lines need to overcome a larger force barrier in order to move out.

One can also see from Fig.4.11, that when a vortex is not too close to an inclusion, the force it experiences has a very weak dependence on inclusion radius. This means that when the applied field is not too high, inclusions may not alter the vortex lattice structure significantly.
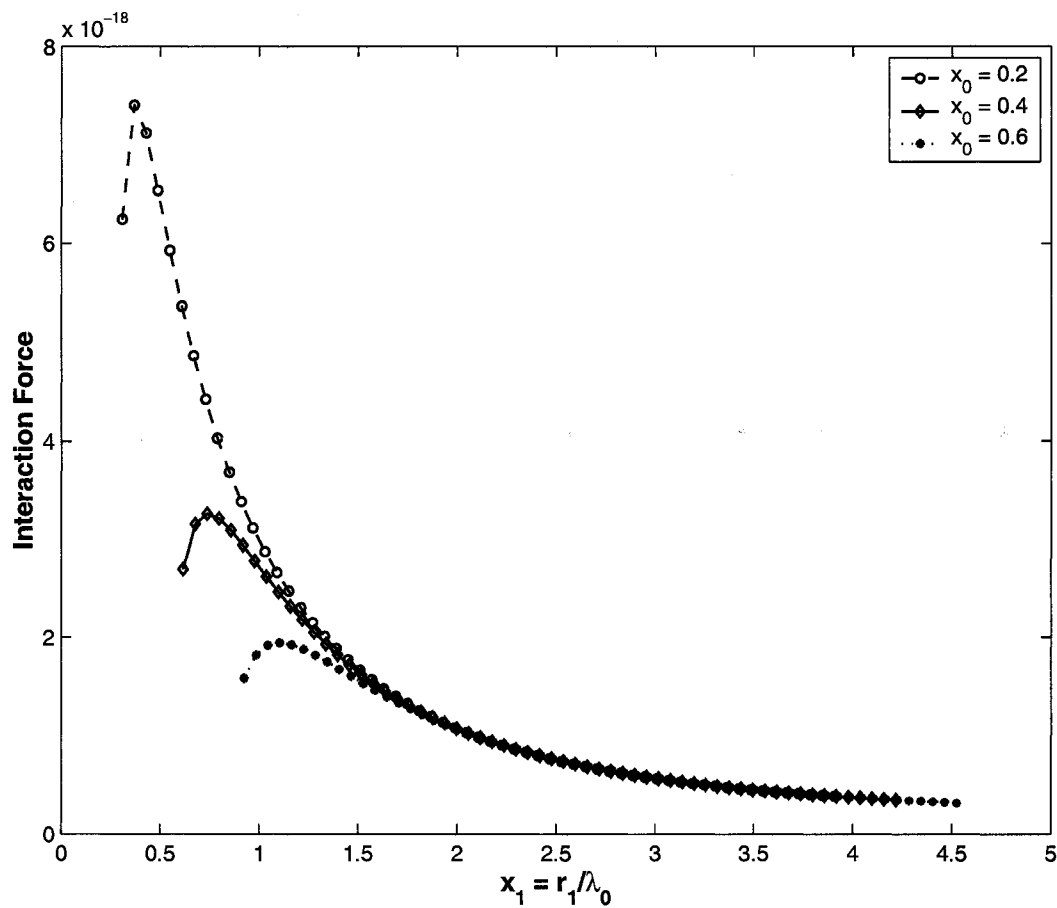
Figure 4.11: Interaction forces(relative value)between an infinitely long cylindrical non-conducting inclusion and a neighbor vortex. For several inclusion radii($x_0 = r_0/\lambda(0)$), the forces experienced by vortex located at x_1 are plotted as function of vortex separations x_1.

Chapter 5

Inclusions in an hexagonal array of vortices

We now generalize to the case where an inclusion, containing at least one quantum of flux, is surrounded by an hexagonal array of vortices – see figure 5.1.

The model described below is based on the London equation with the following assumptions: 1. The "green phase" inclusions are cylindrical and infinite in length; 2. They are non-conducting; 3. They do not change the overall vortex lattice structure so that the near neighbors are still hexagonally arranged; 4. For a given temperature, the more distant vortices contribute a constant average field within the hexagonal array shown in Fig. 5.1; this constant field is ignored in the model.

The assumptions 1 and 2 are basic assumptions of the model, and are generic. Assumptions 3 and 4, as one can see in Chapter 6 where the model is compared with the μSR experiment, are good approximations for lower applied field cases. When the applied field is too high, for example when vortex spacing is less than the penetration depth, assumptions 3 and 4 may need to be modified. Also, since inclusions provide strong pinning, possible temperature modification of the vortex density is not considered in our model.

5.1 Magnetic field

The magnetic field inside non-conducting inclusions is produced by the surrounding supercurrents since there are no currents inside. It is again required that the perpendicular component of current at the cylindrical boundary is zero. For an infinitely long cylindrical inclusion with axis along $\hat{z}$, from symmetry considerations, as shown in Chapter 3, the magnetic field inside the inclusion has only a $\hat{z}$ component and has no θ dependence. Also, this boundary condition requires that the magnetic field $h(r)$ be constant on the boundary and inside the inclusion(see Chapter 4).
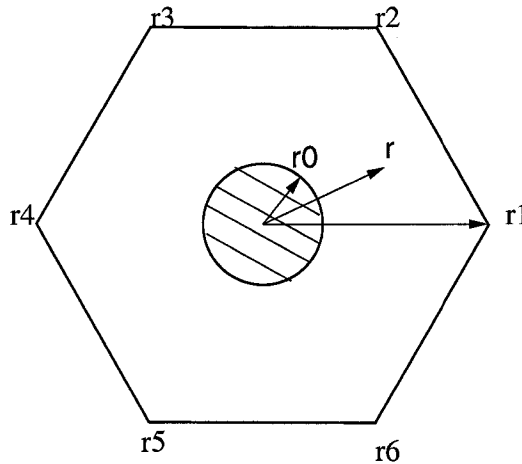
Figure 5.1: An infinitely long cylindrical non-conducting inclusion of radius r_0 in an hexagonal array of superconducting vortices. These vortices are located at $\vec{r}_1, \vec{r}_2 ... \vec{r}_6$.

Without inclusions, the vortices would likely form the hexagonal flux-line lattice predicted by Abrikosov [3]. The inclusion of interest thus has six nearest neighbor vortices which are assumed not to thread inclusions. These six superconducting vortices are located at $(r_i, (i-1) \cdot \pi/3)$ for $i = 1 \ldots 6$ and all $|r_i|$ are equal, as in Fig.5.1. While the magnetic field inside an inclusion is constant, the field outside has contributions from the supercurrents

surrounding the inclusion as well as from the neighboring vortices. This field satisfies the
London equation and boundary conditions:

$$\vec{h}_{in} = \vec{h}_0 \qquad (r < r_0); \tag{5.1}$$

$$\nabla^2 \vec{h}(r, \theta) + \frac{1}{\lambda^2} \vec{h}(r, \theta) = \frac{\vec{\Phi}_0}{\lambda^2} \delta(r - r_i) \qquad (r > r_0); \tag{5.2}$$

$$\vec{h}(r, \theta)|_{r_0} = \vec{h}_0, \tag{5.3}$$

where h_{in} is the field inside the inclusion of radius $\vec{r}_0$, and Φ_0 is the flux quantum. For an
infinitely long cylindrical inclusion, this problem can be solved in two dimensional space.

In the superconducting region between the inclusion and its six neighbor vortices, i.e.
$r_0 < r < r_i (i = 1, 2, ..., 6)$, Eq.5.2 becomes homogeneous. The magnetic field in this
superconducting region between r_0 and r_i can then be conveniently written as:

$$\vec{h}_{sc}(r, \theta) = \vec{h}_{out}(r, \theta) + \vec{h}_{vortex}(r, \theta). \tag{5.4}$$

We have

$$h_{in}(r) = h_0 \qquad (r < r_0); \tag{5.5}$$

$$h_{out}(r, \theta) = \sum_m A_m K_m(\frac{r}{\lambda}) e^{im\theta} \qquad (r > r_0); \tag{5.6}$$

$$
\begin{aligned}
h_{vortex}(r, \theta) &= \frac{\Phi_0}{2\pi\lambda^2} K_0 \left(\frac{|\vec{r_1} - \vec{r}|}{\lambda} \right) + \frac{\Phi_0}{2\pi\lambda^2} K_0 \left(\frac{|\vec{r_2} - \vec{r}|}{\lambda} \right) + ... \\
&+ \frac{\Phi_0}{2\pi\lambda^2} K_0 \left(\frac{|\vec{r_6} - \vec{r}|}{\lambda} \right) \\
&= \frac{\Phi_0}{2\pi\lambda^2} \sum_m I_m \left(\frac{r}{\lambda} \right) K_m \left(\frac{r_1}{\lambda} \right) e^{im\theta} + \frac{\Phi_0}{2\pi\lambda^2} \sum_m I_m \left(\frac{r}{\lambda} \right) K_m \left(\frac{r_2}{\lambda} \right) e^{im\theta_2} + \\
&... + \frac{\Phi_0}{2\pi\lambda^2} \sum_m I_m \left(\frac{r}{\lambda} \right) K_m \left(\frac{r_6}{\lambda} \right) e^{im\theta_6} \qquad (r_0 < r < r_i, i = 1, 2, ..., 6),
\end{aligned}
\tag{5.7}
$$

where $\theta_1 = \theta$, $\theta_2 = |\theta - \frac{\pi}{3}|$, $\theta_3 = |\theta - \frac{2\pi}{3}|$,..., $\theta_6 = |\theta - \frac{5\pi}{3}|$. $\vec{h}_{in}(r)$ is the magnetic field inside the inclusion. $\vec{h}_{out}(r,\theta)$ is the magnetic field outside the inclusion due to the supercurrents surrounding the boundary of the inclusion produced by the flux quanta trapped in the inclusion. $\vec{h}_{vortex}(r,\theta)$ is the magnetic field produced by vortices located at $\vec{r_i}$, i=1,2,...,6.

The magnetic field in the superconducting region between r_0 and r_i is the superposition of $\vec{h}_{out}(r,\theta)$ and $\vec{h}_{vortex}(r,\theta)$, as described in Eq.5.4.

Since $r_1 = r_2 = ... = r_6$, we can rewrite h_{vortex} as

$$h_{vortex}(r,\theta) = \frac{\Phi_0}{2\pi\lambda^2} \sum_m I_m\left(\frac{r}{\lambda}\right) K_m\left(\frac{r_1}{\lambda}\right) \left(e^{im\theta_1} + e^{im\theta_2} + ... + e^{im\theta_6}\right). \qquad (5.8)$$

The magnetic field in the superconducting region is

$$\vec{h}_{sc}(x,\theta) = \vec{h}_{out}(x,\theta) + \vec{h}_{vortex}(x,\theta) = \sum_m A_m K_m(x)e^{im\theta} +$$

$$\frac{\Phi_0}{2\pi\lambda^2} \sum_m I_m\left(\frac{r}{\lambda}\right) K_m\left(\frac{r_1}{\lambda}\right) (e^{im\theta_1} + ... + e^{im\theta_6}) \qquad (r_0 < r < r_i), \qquad (5.9)$$

where $x_0 = r_0/\lambda(0)$, $x = r/\lambda(0)$ and $x_i = r_i/\lambda(0)$, i=1,2,...,6.

Applying the boundary condition

$$\vec{h}_{sc}(x)|_{x_0} = \vec{h}_0, \qquad (5.10)$$

we have

$$A_0 = \frac{1}{K_0(x_0)}\left(h_0 - \frac{\Phi_0}{2\pi\lambda^2}I_0(x_0)K_0(x_1)\right) \qquad m = 0 \qquad (5.11)$$

$$A_m = \frac{-1}{K_m(x_0)}\frac{\Phi_0}{2\pi\lambda^2}I_m(x_0)K_m(x_1)\left(1 + e^{im\theta_2-\theta} + ... + e^{im\theta_6-\theta}\right) \qquad m \neq 0. \qquad (5.12)$$

The magnetic field in the superconducting region can then be written as

$$
h_{sc}(x) = \frac{h_0 K_0(x)}{K_0(x_0)} +
$$
$$
\frac{\Phi_0}{2\pi\lambda^2} \sum_m \left(\frac{-I_m(x_0)K_m(x_1)}{K_m(x_0)} K_m(x) + K_m(x_1)I_m(x) \right) \left(e^{im\theta_1} \right.
$$
$$
\left. + e^{im\theta_2} ... + e^{im\theta_6} \right), \tag{5.13}
$$

where $h_0 = constant$ is the magnetic field inside the inclusion – its value will be determined

by the fluxoid quantization condition. The sum of index m is running from $-\infty$ to $+\infty$.

Magnetic Field Distribution
(Applied Field is around 300 Gauss)

$r_0 = 290 \, A^0$
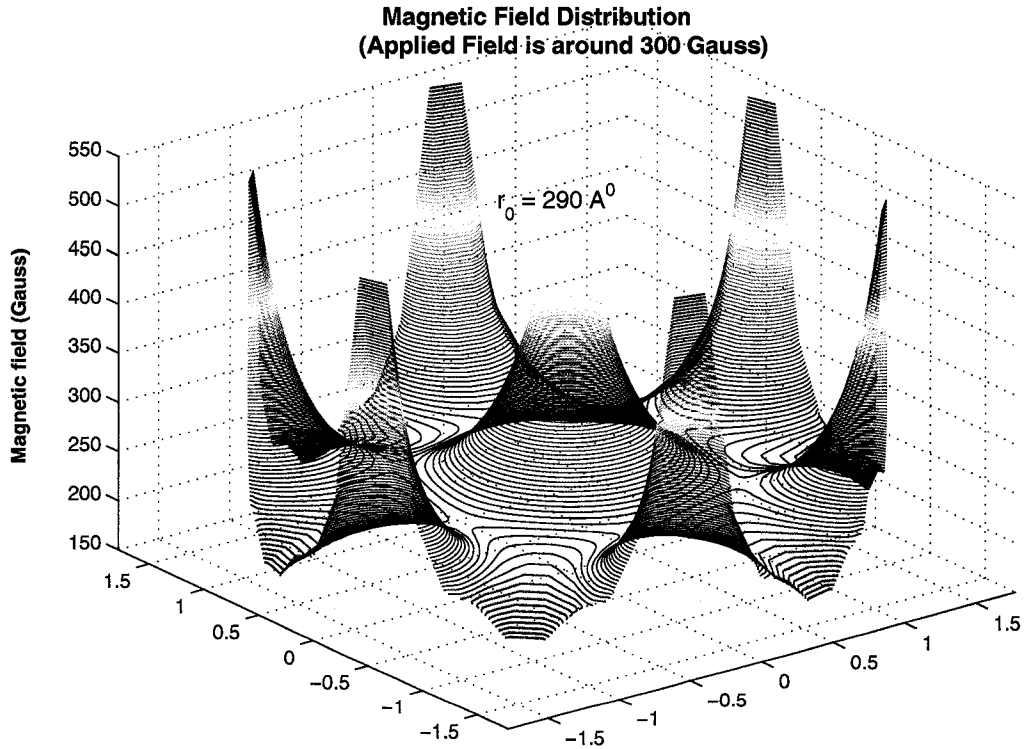
Figure 5.2: 3D contour plot of the magnetic field distribution of a cylindrical inclusion in hexagonal array of normal vortices near lower critical field h_{c1}. The penetration depth is 1450 $\overset{\circ}{A}$.

In 2D polar coordinates, the fluxoid quantization can be written as

$$\Phi + \lambda^2 \oint r_0(-\frac{\partial h}{\partial r})d\theta = n\Phi_0. \tag{5.14}$$

We'll insert h_{sc} into the above fluxoid quantization condition to determine h_0. When $m \neq 0$,

the integration over θ gives

$$\oint e^{im\theta_i}d\theta_i = 0, \qquad i = 1, 2, ...6. \tag{5.15}$$

Carrying out the integration over θ we get:

$$\pi r_0^2 h_0 - 2\pi\lambda x_0 \frac{h_0}{K_0(x_0)}K_0'(x_0)$$
$$+ 6\Phi_0 x_0 \left(I_0'(x_0)K_0(x_1) - \frac{I_0(x_0)K_0(x_1)}{K_0(x_0)}K_0'(x_0) \right) = n\Phi_0. \tag{5.16}$$

Solving the above equation we get the expression for h_0

$$h_0 = \frac{\Phi_0}{2\pi\lambda^2 x_0} \frac{nK_0(x_0) + 6K_0(x_1)}{K_1(x_0) + \frac{x_0}{2}K_0(x_0)}. \tag{5.17}$$

Comparing with Eq.4.54, we see that in hexagonal array all six neighbor vortices have

contributions to the magnetic field inside the inclusion. Therefore, h_0 will be higher in an

hexagonal array than that given by Eq.4.54 where there is only one vortex neighbor.

The 3D magnetic field distribution of a cylindrical inclusion in hexagonal array of vor-

tices is shown in Fig.5.2. The external magnetic field was chosen to be higher than the

lower critical field H_{c1}, around 300 Gauss for $YBa_2Cu_3O_{7-\delta}$. The vortex separation near

H_{c1} is given by $d = \sqrt{2}\Phi_0/\sqrt{3}B_{c1})$, where B is the average field, which gives $d = 1.78\lambda_0$.
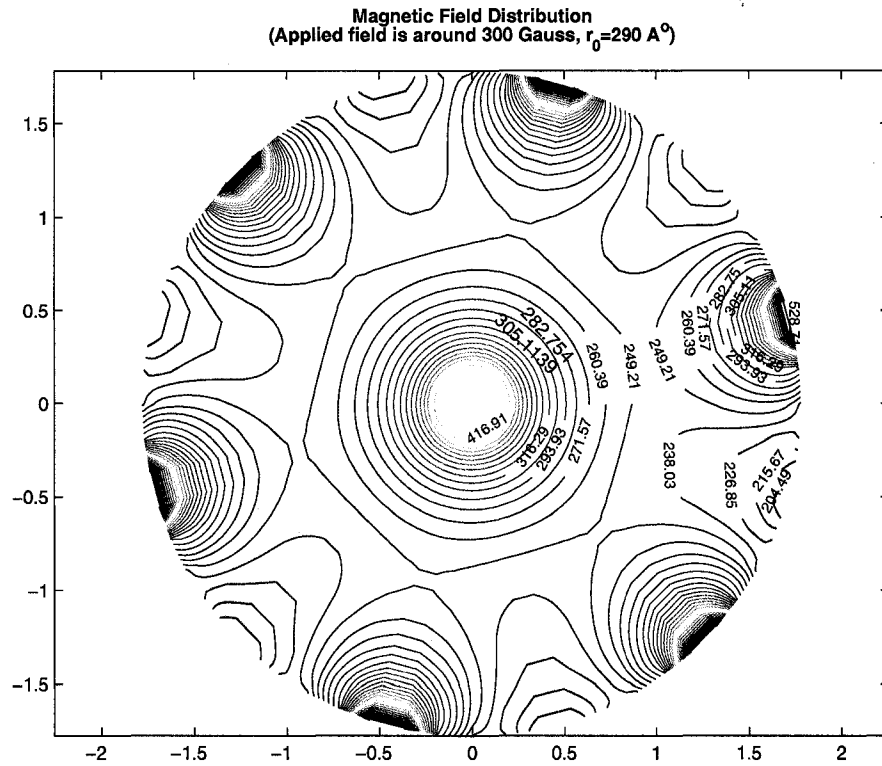
Figure 5.3: Magnetic field distribution of a cylindrical inclusion in hexagonal array of vortices near lower critical field h_{c1}. The radius of the inclusion is 390 $\mathring{A}$. The penetration depth is 1450 $\mathring{A}$.

So we have $x_1 = r_1/\lambda_0 = 1.78$ and $x_0 = r_0/\lambda_0 = 0.2$. A single flux quantum was assumed to thread the inclusion.

Fig.5.3 portrays in 2D space the magnetic field distribution of a cylindrical inclusion in an hexagonal array of vortices when the applied field is higher than the lower critical field H_{c1}. Along the path from the center of the inclusion to the next vortex, the 2D contour plot clearly shows the saddle points.

Along the direction from the center of the inclusion to a next neighbor vortex in the hexagonal array, we get a one dimensional field distribution where the lowest point corresponds to the saddle point, see Fig.5.4. It is interesting to see again that the radius
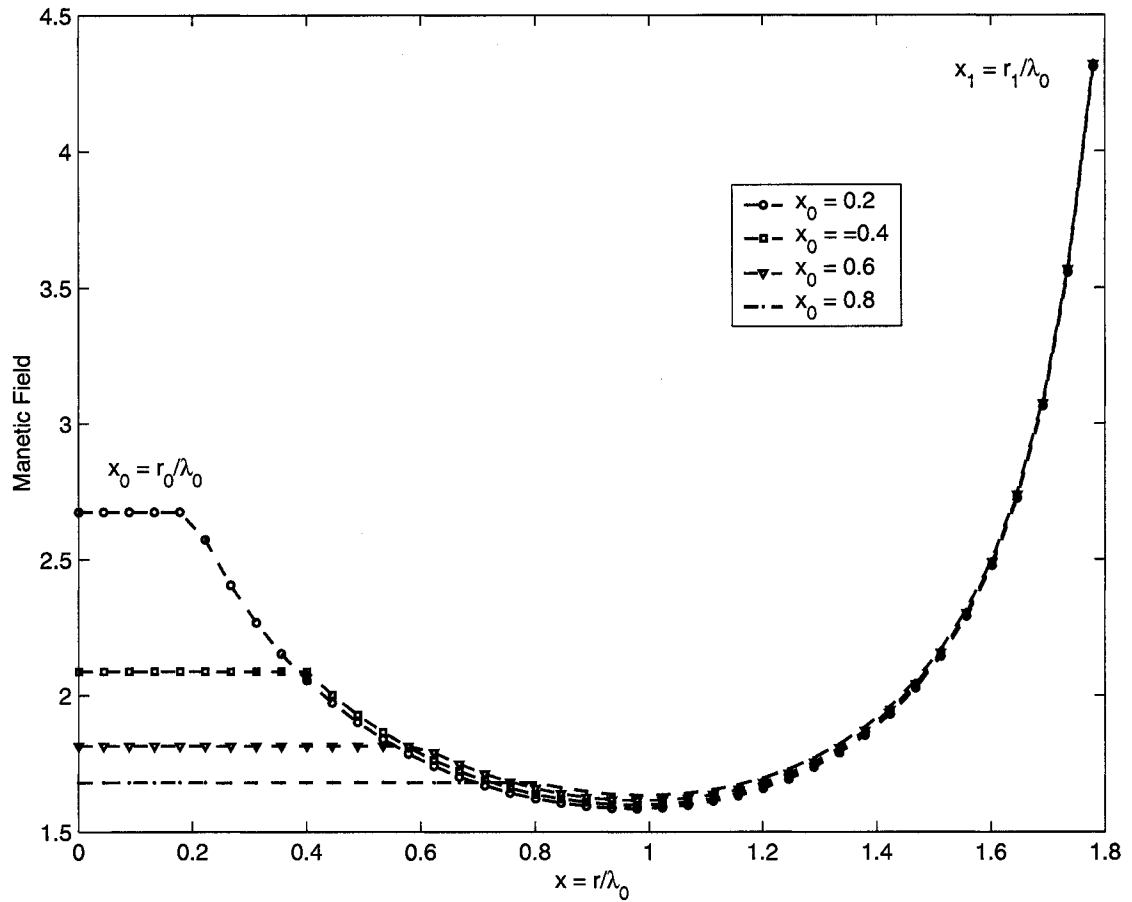
Figure 5.4: Relative values of the magnetic field in the superconducting region outside of the inclusion in hexagonal array of vortices as function of $x = \frac{r}{\lambda(0)}$. The field is shown in the direction of $\theta = 0$. $x_0 = \frac{r_0}{\lambda(0)}$, where r_0 is the radius of inclusion. The minimum field correspond to the saddle point.

of the inclusion has little impact on the field distribution in the superconducting regions.

As discussed in the previous chapter, this means that the average field is not sensitive to changes in inclusion radius when the applied field is low. Therefore the saddle point is approximately at the same position for inclusions of different radii.

5.2 The Magnetic field probability distribution of a cylindrical inclusion in a hexagonal array of vortices

The probability density function $n(h)$ is usually chosen so that $n(h)dh$ gives the probability that, when randomly sampling over a unit cell of the vortex lattice, one will find the local magnetic field to be between h and $h + dh$. Here we used for our unit cell the area shown with contours in Fig. 5.3. It is defined so that $\int_0^\infty n(h)dh = 1$, and $\int_0^\infty n(h)hdh = h_{ave}$, where h_{ave} is the average field.

When the applied field is low ($h \ll H_{c2}$), the contribution from the vortex core of radius of order ξ–the superconducting coherence length, is negligible and the magnetic field distribution is little changed for any reasonable value of ξ. Therefore we choose an arbitrarily small value for ξ. The magnetic field spatial distribution of an ideal flux line lattice is given by:

$$h(\vec{r}) = h_{app} \sum_{\vec{k}} \frac{exp[-i\vec{k} \cdot \vec{r}]}{1 + k^2\lambda^2}, \tag{5.18}$$

where h_{app} is the applied field and $\vec{k}$ are the reciprocal lattice vectors.

The field probability distribution, $n(h)$, of the ideal lattice without inclusions is shown in the bottom graph of Fig.5.5. Field distributions closely related to this have been observed in μSR experiments[36, 37, 38, 39]. The maximum field h_{max} corresponds to the field in the small vortex cores of radius of coherence length ξ, which have the highest field. Muons have small probability of seeing these maximum fields since the cores have small relative areas. The minimum field h_{min} is the field in the superconducting areas far away from the cores. The sharp peak in the distribution corresponds to the saddle point field.
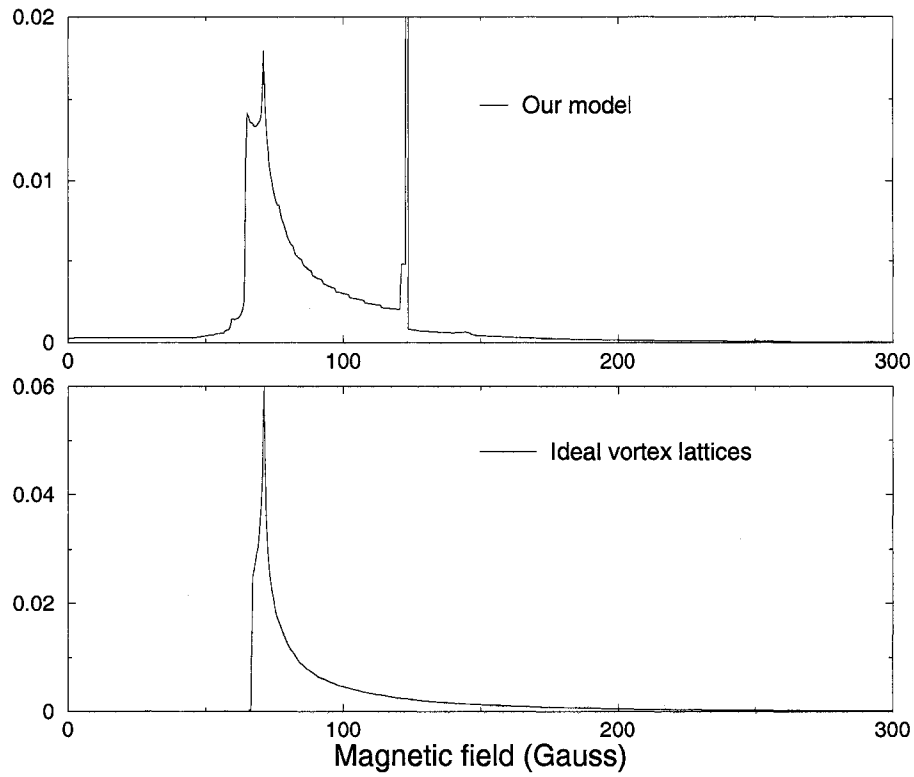
Figure 5.5: Top: Magnetic field probability distribution of cylindrical inclusion in hexagonal array of vortices. The inclusion radius was chosen to be $r_0 = 1200\text{Å}$. Bottom: Magnetic field probability distribution based on isotropic London model for an ideal triangle lattice. The external field was 100 Gauss for both cases.

The top graph of Fig.5.5 shows the magnetic field probability distribution obtained with our model system of an infinitely long cylindrical inclusion surrounded by 6 superconducting vortices using Eq. 5.7 and 5.17 in an applied field of 100 Gauss parallel to the crystal **c** axis. In addition to all the features of a field distribution of an hexagonal lattice of vortex lines, it has a sharp peak above the applied field that corresponds to the field inside the inclusion. The position of this peak is a function of the inclusion radius. Therefore, presuming one has a good estimate of the penetration depth, the position of this peak in the experiment, see Fig.1.1, tells us the average size of the inclusions. The relatively broad distribution of

the right peak in the experiment reflects the distribution of inclusion radii.

That we use an hexagonal array of superconducting vortices for our field calculations, see Fig.5.1 and Fig.5.3, rather than a proper unit cell, and only consider the nearest vortices, leads to an enhanced area associated with the minimum field. This leads to the minimum field peak in the top portion of Fig. 5.5 rather than the shoulder seen in the lower portion. The drop off above the inclusion field seen for our calculation, again as compared with that of a regular vortex lattice field distribution, has the same origin.

Combining Fig.5.4 and the top graph of Fig.5.5, we can see clearly that the second peak in the field probability distribution corresponds to the constant magnetic field in the inclusion area; see Fig.5.6.
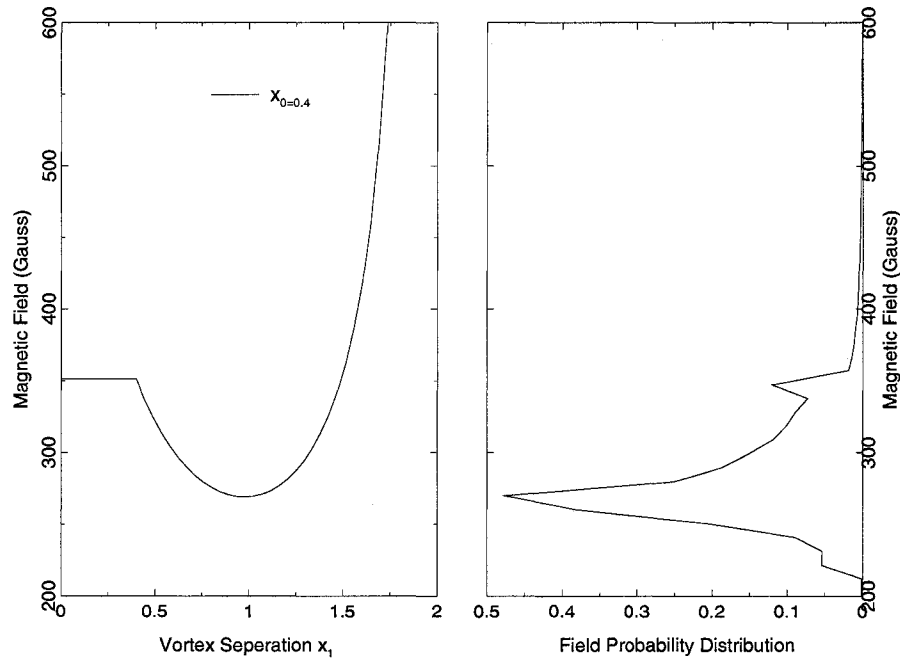
Figure 5.6: Left: Magnetic field from center of inclusion to the near by normal vortex core. Right: Magnetic field probability distribution. The inclusion radius was $x_0 = r/\lambda_0 = 0.4$.

Our model considers only a cylindrical inclusion and its six closest neighbors. Yet if we

compare the top and bottom graphs of Fig. 5.5, we can see that saddle points of the model and that of ideal triangle lattice are almost identical, and that the overall shape of the field distribution in superconducting regions is similar. Thus most of the field distribution is the same with or without the inclusions, the effect of the inclusions is mostly to produce a second peak as observed in the experiment.

5.3 The magnetic field energy of a cylindrical inclusion in an hexagonal array of vortices

When a non-conducting inclusion is placed in an hexagonal array of vortices, the magnetic field energy per unit length of a cylindrical inclusion includes the magnetic field energy of the inclusion, the magnetic field energy in the superconducting region and the kinetic energy of currents. The energy can be expressed as

$$
\begin{aligned}
E &= \frac{1}{8\pi} \int_{r<r_0} h_0^2 dS + \int \left(\frac{h^2}{8\pi} + \frac{1}{2} m v_s^2 n_s \right) dS \\
&= \frac{1}{8} r_0^2 h_0^2 + \frac{1}{8\pi} \int_{r>r_0} \left(h^2 + \lambda^2 \left(\nabla \times h^2 \right) \right) dS
\end{aligned}
\tag{5.19}
$$

Here $h(r)$ is the magnetic field in the superconducting region that includes contribution from neighbor vortices and supercurrents surrounding the inclusion. The first integral gives the magnetic field energy inside the inclusion. The integration area of the second integral includes the vortices located at r_i, $i = 1, 2, ..., 6$. Using the London equation, the second and third integrals give:

$$
\begin{aligned}
E_1 &= \frac{1}{8\pi} \int_{r>r_0} \left(h^2 + \lambda^2 (\nabla \times h)^2 \right) dS \\
&= \frac{1}{8\pi} \int \left(\vec{h} + \lambda^2 \nabla \times \nabla \times \vec{h} \right) \cdot \vec{h} dS + \frac{\lambda^2}{8\pi} \oint \left(\vec{h} \times (\nabla \times \vec{h}) \right) \cdot d\vec{S} \\
&= \frac{1}{8\pi} \int_{r>r_0} \Phi_0 h \left(\delta_2(r_1, 0) + \delta_2(r_2, \pi/3) + ... + \delta_6(r_1, 5\pi/3) \right) dS \\
&\quad + \frac{\lambda^2}{8\pi} \oint \left(\vec{h} \times (\nabla \times \vec{h}) \right) \cdot d\vec{S}.
\end{aligned}
\tag{5.20}
$$

The first integral in the above equation is integrated over an area S that includes vortices at (x_i, θ_i); doing so with the help of Eq.5.13 gives:

$$\frac{1}{8\pi} \int_{r>r_0} \Phi_0 \left(h(x_1,\theta)\delta_2(x_1,0) + \ldots + h(x_6,\theta)\delta_6(x_1,5\pi/3) \right) dS$$

$$= \frac{3\Phi_0 h_0}{4\pi} \frac{K_0(x_1)}{K_0(x_0)}$$

$$+ \frac{3\Phi_0^2}{8\pi^2\lambda^2} \sum_m \frac{K_m(x_1)}{K_m(x_0)} \left(-I_m(x_0)K_m(x_1) + K_m(x_0)I_m(x_1) \right). \tag{5.21}$$

The surface integral is taken along the inner (cylindrical surface of the inclusion) and the outer boundary of the integration area. Since the outer boundary goes to infinity, the surface integral at the outer boundary makes no contribution. The inner boundary is along the border of cylindrical inclusion, note that $d\vec{S}$ here is pointed to the center of the inclusion. In polar coordinates with $h = h_{sc}$, the second integral gives

$$\frac{\lambda^2}{8\pi} \oint_{r=r_0} r_0 h \frac{\partial h}{\partial r} d\theta = \frac{\lambda^2}{8\pi} x_0 h_0 \left(-\oint \frac{h_0 K_1(x_0)}{K_0(x_0)} d\theta \right.$$

$$\left. + \frac{\Phi_0}{2\pi\lambda^2} \oint \sum_m \left(-\frac{I_m(x_0)K_m(x_1)}{K_m(x_0)} K_m(x_0)' + K_m(x_1)I_m(x_0)' \right) \right)$$

$$(e^{im\theta} + e^{im\theta_2} + \ldots + e^{im\theta_6}) d\theta. \tag{5.22}$$

Since for $m \neq 0$, $\int_0^{2\pi} e^{im|\theta - \frac{n\pi}{3}|} d\theta = 0$, $n = 0, 1, 2, \ldots 5$. We have therefore

$$\frac{\lambda^2}{8\pi} \oint_{r=r_0} r_0 h \frac{\partial h}{\partial r} d\theta$$

$$= -\frac{\lambda^2 x_0 h_0^2 K_1(x_0)}{4K_0(x_0)} + \frac{3x_0 h_0 \Phi_0}{4\pi} \left(\frac{I_0(x_0)K_0(x_1)}{K_0(x_0)} K_1(x_0) + K_0(x_1)I_0(x_0) \right)$$

$$= -\frac{\lambda^2 x_0 h_0^2 K_1(x_0)}{4K_0(x_0)} + \frac{3h_0 \Phi_0}{4\pi} \frac{K_0(x_1)}{K_0(x_0)}. \tag{5.23}$$

The magnetic field energy in the superconducting region then can be written as

$$
\begin{aligned}
E_1 = {} & \frac{\lambda^2 x_0 h_0^2 K_1(x_0)}{4K_0(x_0)} \\
& + \frac{3\Phi_0^2}{8\pi^2\lambda^2} \sum_m \frac{K_m(x_1)}{K_m(x_0)} \left(-I_m(x_0)K_m(x_1) + K_m(x_0)I_m(x_1)\right).
\end{aligned}
\tag{5.24}
$$

The total magnetic energy of an inclusion with 6 neighbor vortices is

$$
\begin{aligned}
E = {} & \frac{\Phi_0^2}{4\pi^2\lambda^2} \left(\frac{1}{8} + \frac{1}{4x_0}\frac{K_1(x_0)}{K_0(x_0)}\right) \frac{(nK_0(x_0) + 6K_0(x_1))^2}{\left(K_1(x_0) + \frac{x_0}{2}K_0(x_0)\right)^2} \\
& + \frac{3\Phi_0^2}{8\pi^2\lambda^2} \sum_m \frac{K_m(x_1)}{K_m(x_0)} \left(-I_m(x_0)K_m(x_1) + K_m(x_0)I_m(x_1)\right).
\end{aligned}
\tag{5.25}
$$

Fig. 5.7 shows the total energy for inclusions of several radii in an hexagonal array of vortices. The energy is plotted as function of vortex separation $x_1 = r_1/\lambda(0)$ for a given inclusion radius $x_0 = r_0/\lambda(0)$. There are similarities and differences between the case of an inclusion in an hexagonal array of vortices and an inclusion with only one vortex neighbor. When the distance between the normal vortex and the inclusion decreases, the interaction energy increases in both cases. However, when one compares Fig. 4.9 with Fig. 5.7 we can see that in an hexagonal array of vortices, the interaction energy is not sensitive to the inclusion radii, while in the case where there is only one vortex neighbor the interaction energy increases when the radius of inclusion decreases. We believe that this is due to the fact that the magnetic field inside the inclusion now has contributions from six neighbors instead of just one neighbor. When a vortex line moves towards an inclusion in hexagonal array of vortices, it needs to overcome forces from all other five vortices, as compared with
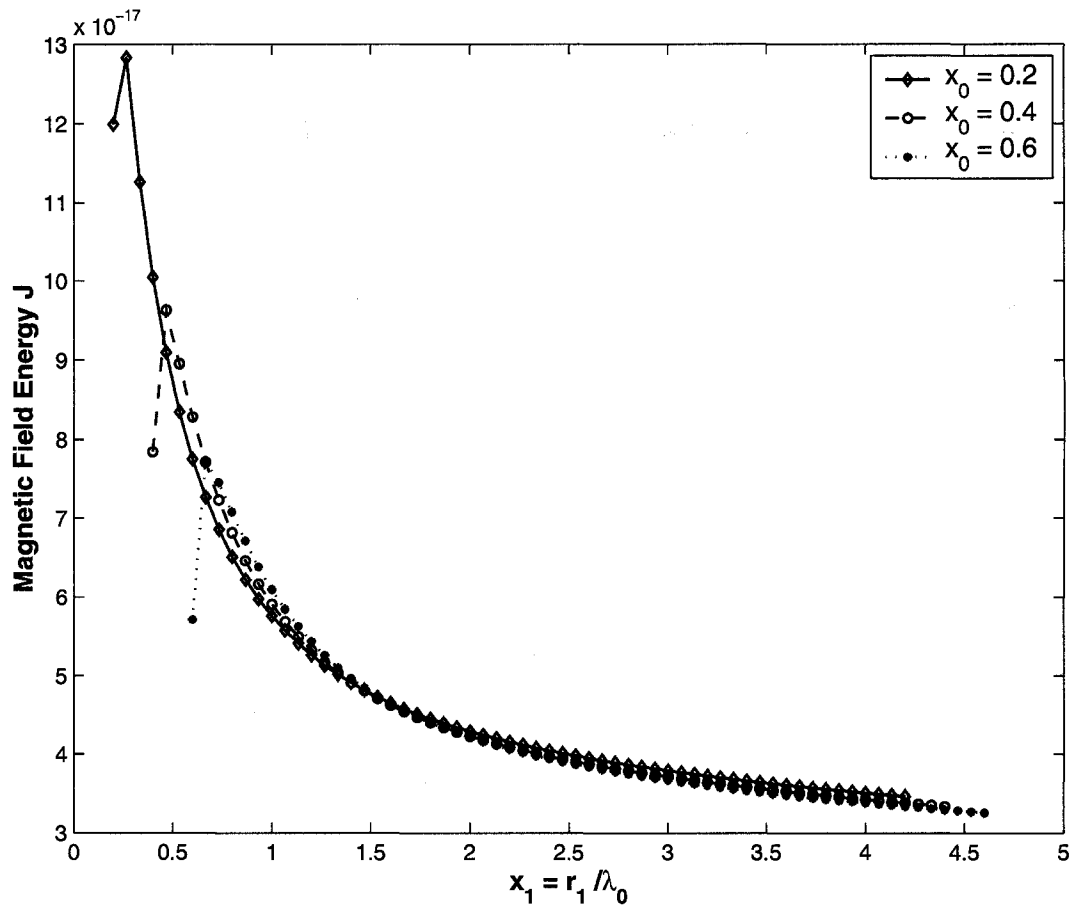
Figure 5.7: Relative values of the total energy of an inclusion among an hexagonal array of vortices. Several radii of inclusions are shown. For a given inclusion radius, the energy is plotted as function of vortex separation x_1.

an inclusion with just one vortex system. Also in this case the impact of self energy of the inclusion on the total energy of the system is lesser than where there is only one vortex neighbor.

5.4 Interaction force between an inclusion and an hexagonal array of vortices

The force between an inclusion and a vortex in an hexagonal array of vortices can be directly obtained from the interaction energy. Assuming the vortex at r_1 moves towards the center of the inclusion along the - $\vec{r_1}$ direction, it experiences a force due to the interaction with the inclusion and the other five vortices in the hexagonal array,

$$F = -\frac{\partial E}{\partial x_1},\qquad(5.26)$$

where E is the total magnetic field energy of inclusion in an hexagonal array of vortices as in Eq.5.25.

In Fig.5.8, vortex spacing x_1 is fixed by the applied field. The force experienced by normal vortex at x_1 of is plotted as function of inclusion radius x_0.

Compare Fig.5.9 with Fig.4.10 one can see that the difference between the energies corresponding $x_1=2.5$ and $x_1=3.5$ is smaller in case that the inclusion is in an hexagonal array of vortices. This is also due to the decreasing of the impact of inclusion self energy on the total energy of the system when there are more then one vortices.

In fig. 5.9, the force experienced by a normal vortex is expressed as a function of vortex separation x_1 for a given inclusion radius. The repulsive force between an inclusive and vortices in an hexagonal array is similar to that for an inclusion with single vortex system as discussed in section 4.4.3. When a normal vortex approaches the inclusion from a distance, the repulsive force increases. For a normal vortex to be trapped into an inclusion,
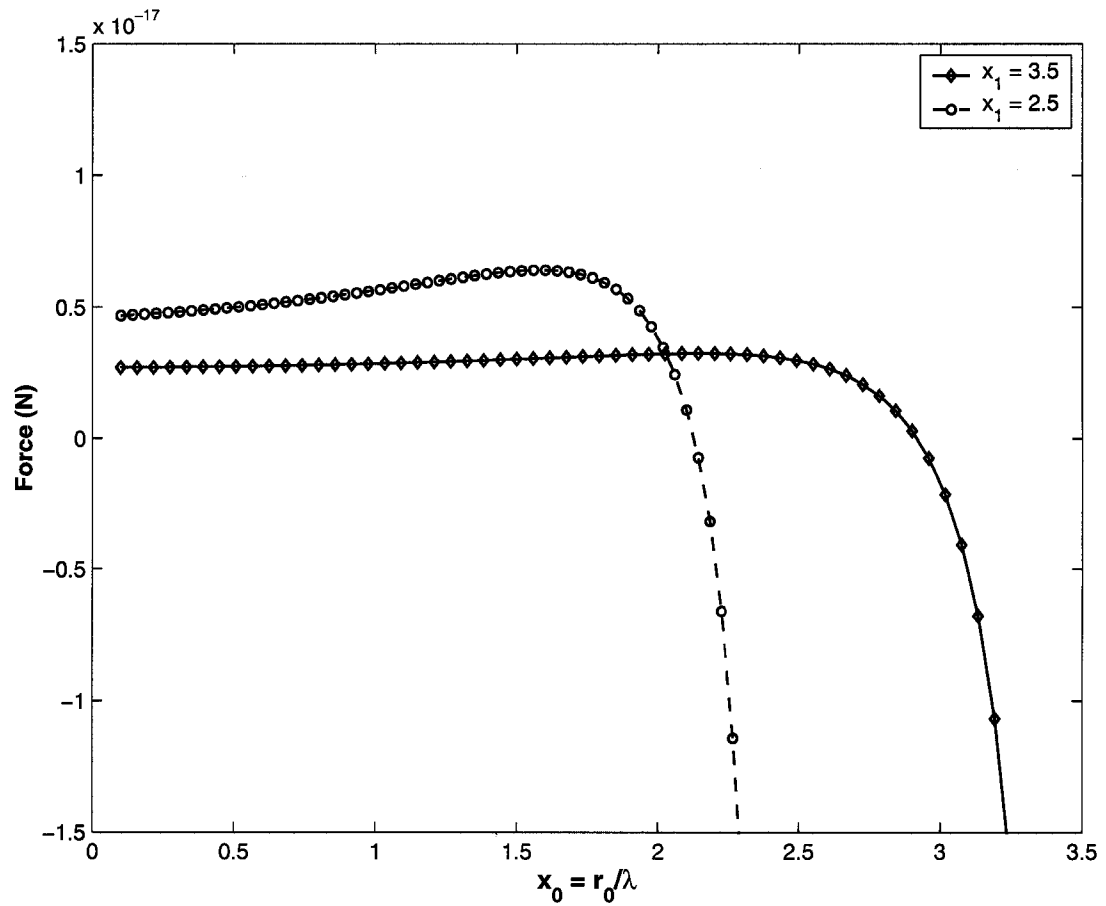
Figure 5.8: Interaction forces(relative value) between infinitely long cylindrical non-conducting inclusion and neighbor vortices in hexagonal lattice. For fixed vortex separation (x_1), the force experienced by vortex located at x_1 is plotted as function as inclusion radius x_0.

it must overcome a force barrier. This force barrier decreases as the radius of the inclusion increases. It is energetically easier for large inclusions to contain multiple flux quanta as compared to smaller inclusions.
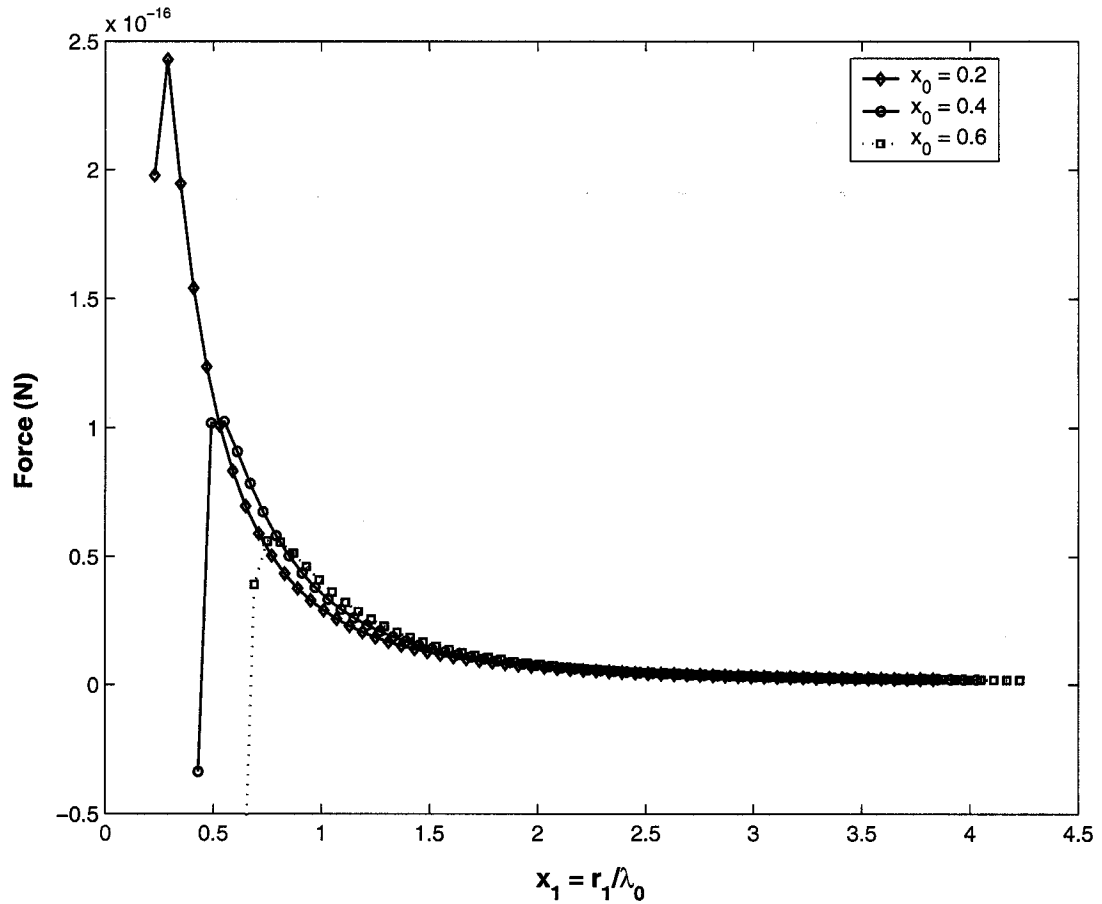
Figure 5.9: Interaction forces(relative value)between infinitely long cylindrical non-conducting inclusion and neighbor vortices in hexagonal lattices. For several inclusion radius (x_0) values, the forces experienced by vortex located at x_1 are plotted as function of vortex separations x_1 (distance between vortex and the center of inclusion).

5.5 Non-interaction Model

In section 4.1, we have discussed the situation that a isolated vortex line is trapped in the cylindrical non-conducting inclusion. The magnetic field inside and outside of the inclusion is expressed in Eq. 4.27 and Eq. 4.28 respectively.

In section 5.1, we have considered the case that the inclusion is placed in an hexagonal array of vortices. The interaction between the inclusion and its six vortices neighbors has

been considered to get the magnetic field distribution inside and outside of the inclusion, see Eq.5.13 and Eq. 5.17.

When the applied magnetic field is weak, the interaction between the inclusion and its neighboring vortices can be ignored. In this non-interaction model, the magnetic field in the superconductor is simply the superposition of the field distribution for a vortex threading an isolated inclusion and the field of single vortices located at r_1 through r_6.

Referring to equations 4.27, 4.28, 4.41 and 3.19, we see that the magnetic field distribution inside and outside of the inclusion in the non-interaction model can be written as

$$h_0 = \frac{\Phi_0}{2\pi\lambda^2 x_0} \frac{nK_0(x_0)}{K_1(x_0) + \frac{x_0}{2}K_0(x_0)}, \tag{5.27}$$

and

$$
\begin{aligned}
h_{out} =\ & \frac{\Phi_0}{2\pi\lambda^2 x_0} \frac{nK_0(x)}{K_1(x_0) + \frac{x_0}{2}K_0(x_0)} \\
& + \frac{\Phi_0}{2\pi\lambda^2} \sum_m I_m\left(\frac{r}{\lambda}\right) K_m\left(\frac{r_1}{\lambda}\right)\left(e^{im\theta_1} + ... + e^{im\theta_6}\right) \quad (r_0 < r < r_i).
\end{aligned}
\tag{5.28}
$$

The magnetic field distribution for an inclusion of radius 1200 $\overset{\circ}{A}$ among six vortices in an hexagonal array is shown in Fig. 5.10. The applied magnetic field is 100 Gauss. The penetration depth is 1450 $\overset{\circ}{A}$. For comparison, the field distribution is calculated here using a method that considers the interactions between the inclusion and its neighboring vortices as in section 5.1, and the results are shown in Fig. 5.11.

We can see that when the applied field is low, the overall field distribution given by the non-interaction model in Fig. 5.10 is similar to that in Fig. 5.11 where the interaction
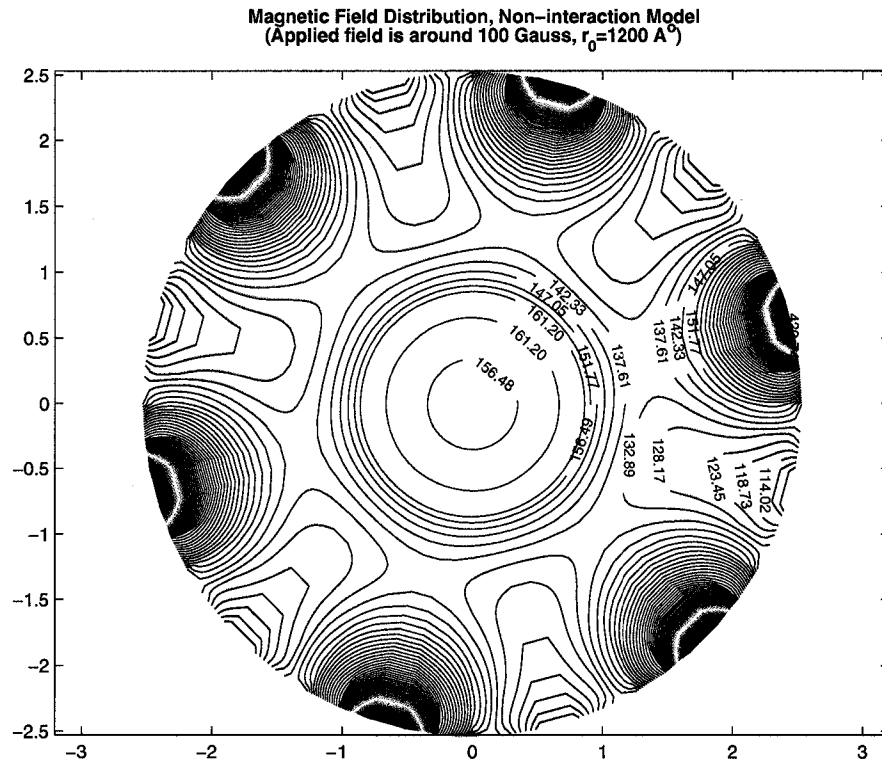
Figure 5.10: Magnetic field distribution of a cylindrical inclusion in hexagonal array of vortices in non-interaction model. The applied field is around 100 Gauss. The radius of the inclusion is chosen to be 1200 $\overset{\circ}{A}$. The penetration depth is 1450 $\overset{\circ}{A}$.

has been considered. Since the non-interaction model does not consider correct boundary conditions, the field inside of the inclusion is no longer constant. The similarity implies that at low fields superposition of fields for a vortex threading spherical inclusions and fields from surrounding normal vortices may be close to the fields appropriates to this geometry.

Magnetic Field Distribution
(Applied field is around 100 Gauss, r_0=1200 A$^{\circ}$)
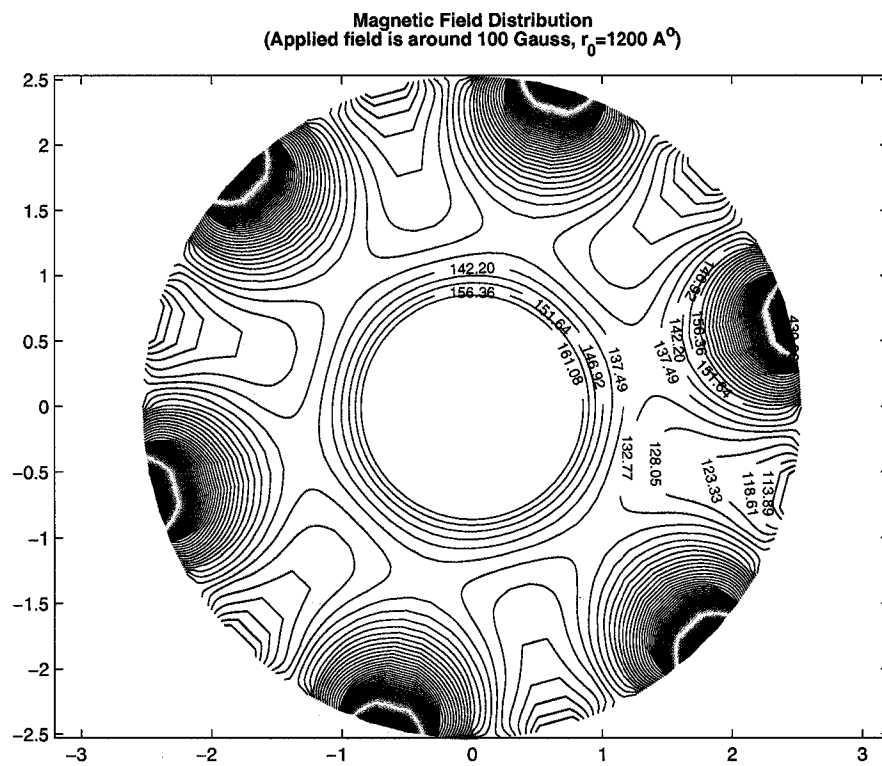
Figure 5.11: Magnetic field distribution of a cylindrical inclusion in hexagonal array of vortices in interaction model as discussed in section 5.1. The applied field is around 100 Gauss. The radius of the inclusion is chosen to be 1200 Å.

Chapter 6

Comparison with μSR experiments

In this chapter we compare the calculated internal magnetic field in the cylindrical non-conducting inclusion with the measured results from μSR experiments. We use the model developed in the previous Chapters to calculate the magnetic field probability distribution inside the inclusion and in the superconducting regions. By analyze the temperature evolution of the two peaks of the magnetic field probability distributions in the inclusion and superconducting regions and compare them with the temperature dependent peaks positions from μSR experiment, we can directly obtain the temperature dependence of the penetration depth $\lambda(T)$.

6.1 Sample Preparation

The sample was grown using a single crystal, $SmBa_2Cu_3O_{7-x}$ (SBCO) seed to induce crystallization during the melt-growth process, similar to that demonstrated by Murakami, et al.[11]. The SBCO seed was grown with the a-b plane parallel to the surface. A disk made from melt quenched powders was melt-processed, yielding a single crystal extending to the edge of the sample. No low angle or high angle grain boundaries were observed

83

as determined by SEM, high resolution TEM, and x-ray analysis. Crystals up to 5 cm in diameter have been grown by this technique.

Addition of excess Y_2BaCuO_5 (211 or the green phase) helps in the crystal growth kinetics. At high temperatures, the sample consists of a liquid phase plus 211 particulates. As the crystal nucleates, the grain begins to grow and 123 solidifies, consuming most of the 211 phase. However, some of the 211 particulates become encapsulated before they are consumed. An excess of 211 is necessary to continue grain growth over a large area since, if excess 211 is not present, the continued growth of 123 is arrested by yttrium depletion prior to 123 formation throughout the entire sample. The fractional content of 211 is between 0.1 and 0.5 for typical samples. These inclusions are thought to strongly pin the vorticies associated with the internal magnetic field.

6.2 Model

μSR and analysis techniques has been discussed in detail in Chapter 2. We are going to use model developed in the previous Chapters to compare with the μSR experimental data. Using Eqs. 5.2 and 5.7 to calculate the magnetic field distribution, we get the field probability distributions shown in the lower portion of Fig.6.1. The field distribution depends on the penetration depth, λ, the inclusion radius and the vortex separation. For comparison, the Fourier transform of μSR data taken on $YBCO$ at 18 K is shown in the upper portion of the same graph.

The vortex spacing is determined by the applied field. For an hexagonal lattice of vortices, the average field h_{ave} is given by[41]

$$h_{ave} = \frac{2\Phi_0}{\sqrt{3}r_1^2}.\tag{6.1}$$

h_{ave} can be measured from μSR data, or calculated based on Eq.5.3 and 5.7. The μSR data (Fig.1.1) gives the average field around 91.3 Gauss, which corresponds to a vortex separation $r_1 = 5117\text{Å}$.

Although our model considers only six hexagonally arranged nearest neighbors, the experimentally applied field is so low that the lattice spacing is very large (about 4 times λ_0). So those six vortices are the major contributors to the magnetic field in the neighborhood of the inclusion. Therefore it is appropriate to ignore the contributions from more distant vortices.

One may see that the magnetic field distribution in the superconducting region is not strongly affected by the presence of a large inclusion by considering the results shown in the

lower portion of Fig. 6.1. While varying the radius of the inclusion dramatically changes

the inclusion peak position, the remainder of the distribution is not much affected.
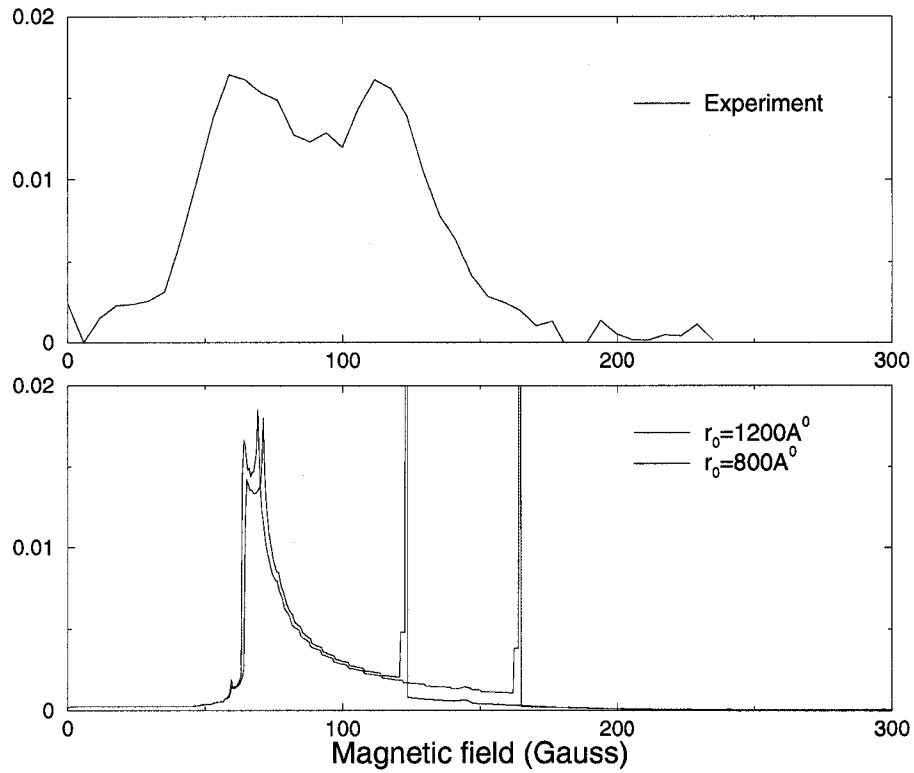
Figure 6.1: Bottom graph: Magnetic field probability distribution of cylindrical inclusions of two different radii in an hexagonal array of vortices. Top graph: Fourier transformation of μSR experiment data. The sample was a thin disk and the external field was approximately 100 Gauss.

6.3   Inclusion Radii and Low Temperature λ

Just below 18 K the second peak disappears due to the anti-ferromagnetism in the "green phase material". From this lower temperature data we determined λ at 16 K by fitting our μSR data to a function related to Eq.5.18. This gives λ to be around 1450 Å.

Assuming that $\lambda(16K) \approx \lambda(18K)$ we determine r_0 from $r_0 = x_0 \cdot \lambda$. Two different r_0 values are shown on the graph. We can see that inclusions of radius $r_0 \sim 1200$ Å have their peaks at the corresponding peak of the Fourier transformation of μSR data. We will use this value of inclusion radius for later determination of $\lambda(T)$.

The size of the inclusions is much larger than that of the superconducting vortex core, therefore the introduction of inclusions might cause some distortion to the vortex lattice. However, when the vortex spacing is much larger than the radii of inclusions, which is the case for the low applied magnetic field used here, this distortion should be small. When the applied field is high, the distortion introduced by an inclusion can no longer be neglected.

6.4 Temperature Evolution of the Two Peaks

Figure 6.2 displays the temperature dependent splitting of the experimental peaks. As temperature decreases, the two peaks move apart, i.e., the saddle point peak moves to the left (lower field direction) and the new right peak moves further to the right, i.e., higher field direction. The separation between the two peaks is zero at the transition temperature, increases with decreasing temperature, and reaches 50 Gauss at 18 K. This separation is shown in Fig. 6.2.

The experimental separation between the peaks as a function of temperature is plotted in Fig. 6.2. The smooth curve in that figure corresponds to the separation using our model with $r_0 = 1200\text{Å}$, $\lambda(0K) = 1450$ Å, and the two-fluid[40] temperature dependence of $\lambda(T)$. Note, that we have assumed that $\lambda(0K) \approx \lambda(16K)$, which is certainly true if the two-fluid model is appropriate.
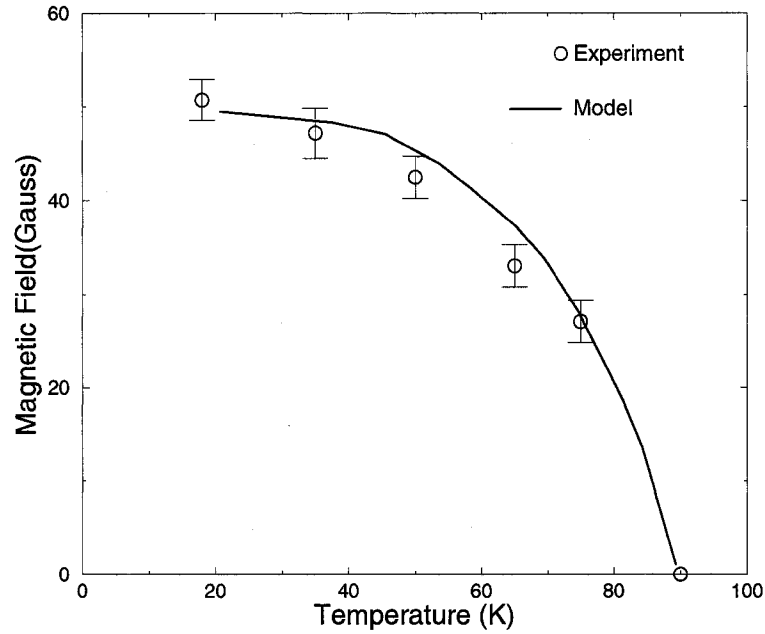
Figure 6.2: Temperature evolution of the separation between the two peaks. The inclusion radius in the model was $r_0 = 1200$Å, and the penetration depth was $\lambda_0 = 1450$Å.

6.5 Temperature Dependence of λ

We can directly obtain the temperature dependence of $\lambda(T)$ from our model and μSR data without using the two-fluid model. The relation between the temperature and penetration depth is determined by comparing the separation of the two peaks obtained from experiment at different temperature to the separation calculated from our model for different penetration depths. Using this relationship we obtain the temperature dependence of the penetration depth, $\lambda(T)$, shown in Figure 6.3.

These data are again compared in Fig. 6.3 to the two fluid model for which we used $\lambda(18K) \approx \lambda(16K)$. The agreement is striking, further justifying our assumption that $\lambda(0K) \approx \lambda(16K)$.
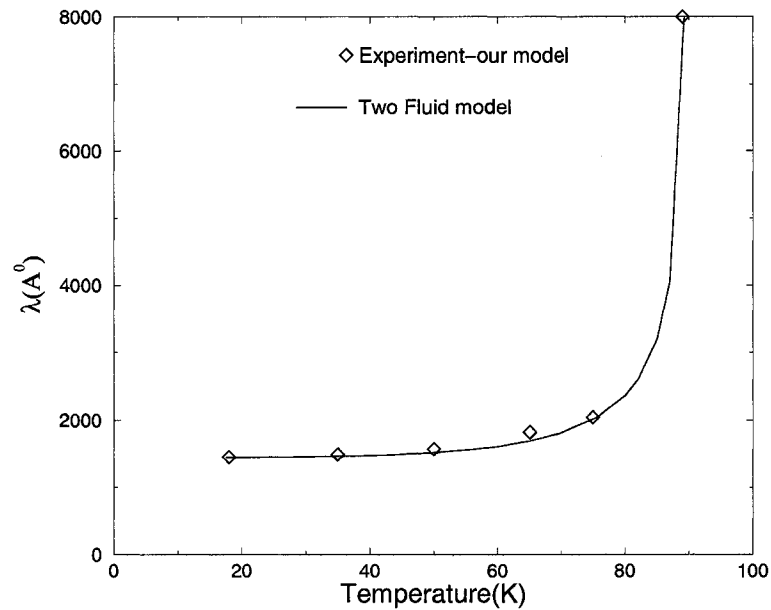
Figure 6.3: Temperatures dependence of the penetration depth. The solid line is obtained from λ_0 and two-fluid model. The diamond points are $\lambda(T)$ directly obtained from the experiment and our model.

It is known that the two fluid model fits well with the powder sample but does not so well with uncorrected data for high quality single crystals. The technique we have developed fits well with the single crystal samples. Since the sample we used has large nonconducting inclusions that cause strong pins, it is expected that its temperature dependence of the magnetic penetration depth to be like powder samples, although it is still a single crystal. Therefore the techniques we have developed especially useful to measure the temperature dependence of London penetration depth for signal crystal samples with strong pins.

6.6 Conclusions

In this study we have characterized the microscopic internal magnetic field distribution of high-T_c superconducting material $YBa_2Cu_3O_{7-\delta}$ with non-conducting inclusions. The magnetic field trapped in inclusions produces a second peak in the Fourier transform of the μSR data above the applied field. We have developed a model based on London equations to account the magnetic field probability distribution inside the inclusion and in the superconducting regions and reproduced the two peaks observed in μSR experiments.

We have also reproduced the temperature evolution of the separation between the two peaks observed in experiment. This separation depends on the inclusion radius and λ_0. From the lower temperature data we determined λ at 16 K by fitting our μSR data to the field of ideal lattices. Assuming that λ (16 K) approx λ (18 K) we determine inclusions radii. If the inclusions' radii are known, fitting the temperature dependent separation between the two peaks provides a new way to measure the temperature dependence of London penetration depth. This new technique is especially useful to study the temperature dependence of London penetration depth of single crystal samples with strong pins.

In many practical applications of high-T_C superconducting materials, column defects are introduced to create strong pinning in order to pin the vortices even when strong currents exert strong force transverse to the vortex axis. This type of materials have strong pinning, can carry large current and trap large filed, therefore it is thought to be advantage for a variety of practical applications. The model we have discussed is suitable to study these types of applications and it may provide a new method to determine the penetration depth of those materials.

Bibliography

[1] W. Meissner, R. Ochsenfeld, Naturwiss. 21, 787, 1933.

[2] , Zh. Eksp. Tero. Fiz. 7, 371, 1937.

[3] A.A Abrikosov: *ZH. Eksp. Tero. Fiz. 32, 1442* (Sov. Phys. -JETP 5, 1174, 1957).

[4] V. L. Ginzburg, L. D. Landau, Zh. Eksp. Tero. Fiz. 20, 1064, 1950.

[5] L. P. Gor'kov Zh. Eksp. Tero. Fiz. 34, 735 (Sov. Phys. -JETP 7, 505, 1958).

[6] Rasetti, F. Phys. Rev. 66, 1-5, 1944.

[7] Lee, T. D., Yang, C. N., Phys, Rev. 104, 254-258, 1956.

[8] Garwin, R. L., Lederman, L. M., Weinrich, M., Phys. Rev. 105, 1415-1417, 1957.

[9] Friedman, J. I., Telegdi, V., L., Phys. Rev. 105, 1681-1682, 1957.

[10] Wu, C. S., Ambler, E., Hayward, R. W., Hoppes, D. D., Hudson, R. P, Phys. Rev., 105, 1413-1415, 1957.

[11] H. Fujimoto *et al.*, in *Melt Processed High Temperature Superconductors*, edited by M. Murakami (World Scientific, Sinseparationore, 1992).

[12] B. Muhlschlegel, Z. Phys. 155, 313 1959.

[13] J.R. Hall, IEEE Spectrum, vol 34, 20, 1997.

[14] Y. Dai, W.J. Kossler, K.G. Petzinger, A.J. Greer, Physica C 402, 263-271, 2004.

[15] A.M. Campbell and D.A. Caldwell, Cryogenics, vol 37, 567, 1997.

[16] A. Weidinger *et al.*, Physica C 143-155, 168, 1988.

[17] C. Meyer *et al.*, Sol. State Comm. 74, 1339, 1990.

[18] I. V. Golosovsky and P.Böni and P. Fischer, Sol. State Comm. 87, 1035, 1993.

[19] R.P. Huebener, *Magnetic Flux Structures in Superconductors* (Springer, 2001).

[20] D.R. Harshman *et al.*, Phys. Rev. Lett. vol 67, 3152, 1991.

[21] S. L. Thiemann, Z. Radović, and V. G. Kogan, Phys. Rev. B 39, 11406 (1989).

[22] A. J. Greer and W. J. Kossler, *Low Magnetic Fields in Anisotropic Superconductors, Lecture Notes in Physics* (Springer, Berlin, 1995).

[23] B.B Goodman Rep. Progr. Phys. 29, 445 (1966)

[24] B. Serin In *Superconductivity*, ed. by R.D. Parks (Marcel Dekker, New York 1969) P.925

[25] F. and H. London, em Proc. Roy. Soc. (London) A 149, 71 (1935).

[26] J.R. Clem Low Temp. Phys. 18, 427 (1975).

[27] Mkrtchyan and Shmidt,Sov. Phys. JETP, 34, p. 195(1972).

[28] Nordborg and Vinokur, Phys. Rev. B, 62, p. 12408 (2000).

[29] C. J. Gorter and H. B. G. Casimir, Phys. Z. 35, 963 (1934); Z. Techn. Phys., 15, 539 (1934).

[30] F. London: *Superfluids, Vol. I* (John Wiley and Sons, New York 1950).

[31] Primakohh, H.,in: V. W. Hughes, C. S. Wu(Eds). *Muon Physics, Vol. 2, Weak Interactions*, pp 3-48, Academic, New York. 1975.

[32] A. Schenck, *Muon Spin Rotation Spectroscopy* (Adam Hilger Ltd, Bristol and Boston, 1985).

[33] J. Chappert, in *Muons and Pions in Materials Research*, edited by J. Chappert and R. I. Grynszpan (North Holland, Amsterdam, 1984), pp. 35–62.

[34] M. Tinkham, *Introduction to Superconductivity, 2nd edition* (McGraw-Hill,1996).

[35] E.M. Forgan *et al.*, Hyp. Int. 105(1997) 61.

[36] D.R. Harshman *et al.*, Phys. Rev. Lett. vol 69, 3313, 1991.

[37] B. Pumpin *et al.*, Phys. Rev. B vol 42, 8019, 1990.

[38] J.E. Sonier *et al.*, Phys. Rev. Lett. vol 72, 744, 1994.

[39] W.J. Kossler *et al.*, Phys. Rev. Lett. vol 80, 592, 1998.

[40] C.J. Gorter and H. Casimirm, Physica vol 1, 306, 1934.

[41] Charles P. Poole Jr. *et al.*, *Suerconductivity* (Academic Press, 1995).

VITA

Yuxin Dai

Yuxin Dai received his B.S. degree from Wuhan University in China and his M.S. degree from Central Michigan University in the U.S.A. After spending two years full time from 1995 to 1997 in the Ph.D. program in the Physics Department of College of William and Mary, he has been working part time on his thesis. During those years from 1997 to 2005 he had been working for optical networking companies such as Nortel Networks and Bell Labs of Lucent. Currently he is working for a startup company in California in the Passive Optical Network (PON) area and involves in the standardization activities of PON at ITU-T (International Telecommunication Union).